이학박사 학위논문

Graphene-Assisted Electron Microscopy for Advanced Chemical & Biological Analysis

그래핀을 응용한 화학적 생물학적 전자현미경 분석에 관한 연구

2015 년 8 월

서울대학교 대학원

화학부 물리화학 전공

박 종 보

그래핀을 응용한 화학적 생물학적 전자현미경 분석에 관한 연구

Graphene-Assisted Electron Microscopy for Advanced Chemical & Biological Analysis

지도 교수 홍 병 희

이 논문을 이학박사 학위논문으로 제출함

2015 년 8 월

서울대학교 대학원

화학부 물리화학 전공

박 종 보

박종보의 이학박사 학위논문을 인준함

2015 년 8 월

위 원 장 정 택 동 (인)

부위원장 홍 병 희 (인)

위 원 민 달 희 (인)

위 원 조 성 표 (인)

위 원 김 근 수 (인)

Ph.D. Dissertation of Science

Graphene-Assisted Electron Microscopy for Advanced Chemical & Biological Analysis

Supervisor: Professor Byug Hee Hong

August 2015

Department of Chemistry

College of Natural Sciences

Seoul National University

Physical Chemistry Major

Jong Bo Park

Abstract

In the 1st part, we demonstrate, for the first time, the liquid phase nanobubbles encapsulated by graphene membrane can be visualized by in-situ UHV-TEM, showing the critical radius of nanobubbles determining its long-term stability as well as two different growth processes of merging nanobubbles depending on their relative sizes. Finally, we confirm that the nanobubbles can catalyze the nucleation and growth of nanoparticles. Our result is believed to provide a deeper understanding on the extraordinary behaviors and functions of nanobubbles.

The behaviors of nanobubbles have been predicted by theoretical studies, but their actual observation with graphene liquid cells needs diverse knowledge and technologies ranging from chemical synthesis, electron microscopy and fluid dynamics to electrochemical and biological approaches. Thus, the present study can be accomplished only by wide interdisciplinary collaboration. In addition, many problems in

our environment are associated with water. Therefore, our finding on new properties and functions of water and nanobubbles will attract immediate concern from the public, which is believed to match well with the scope of a topical, interdisciplinary journal.

In the 2nd part, we found that graphene-coating alternative to metal coating enables non-destructive high-resolution imaging by scanning electron microscopy (SEM) as well as chemical analysis by EDS, utilizing graphene's transparency to electron beams, high conductivity, outstanding mechanical strength, and flexibility. Comprehensive understanding of biological objects can be effectively achieved through electron microscopy (EM) analysis, more effectively without any auxiliary treatment. However, charge accumulation on non-conductive surface by electron beams has always hampered EM-mediated biological studies.

The outstanding performance of atomically thin graphene membrane as protective coating for EM analysis was

theoretically confirmed by Monte Carlo simulations. We believe that the graphene-coated imaging and analysis would provide us a new opportunity to explore various biological phenomena unseen before due to the limitation in sample preparation and image resolution, which will broaden our understanding on the life mechanism of various living organisms.

Keyword : electron microscopy, nanobubbles, scanning electron microscopy, transmission electron microscopy, graphene liquid cells, graphene coating

Student Number : 2012 - 30874

Table of Contents

List of Figures

Figure 16. Direct and indirect gas transport in Ostwald ripening nanobubbles. (a) Schematic representations explaining indirect and direct gas transport. Between two remote nanobubbles, gases are slowly transported through conventional condensation, transmission and evaporation processes, whereas interfacial nanobubbles show direct gas transport through the ultrathin water membrane without hydration. (b) Time-resolved TEM section analysis of the inter-bubble region (line A-B), extracted from a Movie related to Fig. 10a. The thickness of water layer gradually decreases with time, and the occurrences of instantaneous breakjunctions are clearly observed as indicated by white arrows. Opening and closing of water membrane are clearly visible between 11 and 13 s.

Figure 17. Schematic illustration of various biological objects in different scales and coating methods for EM

Figure 22. a-c, Low-magnification FE-SEM images of amorphous carbon-coated ants with different thickness of 2, 10 and 80 nm. Scale bars, 5 μm. **d-f**, High-magnification FE-SEM images of amorphous carbon-coated ants with different thickness of 2, 10 and 80 nm. Scale bars, 500 nm. 2 nanometer-thick carbon film doesn't show good coverage, and it was impossible to obtain high resolution SEM images due to severe charging and blurring effect (**a** and **d**). As the thickness of carbon films increased to 10 and 80 nm, which are normally used for observation of biological specimens, the surface morphology of carbon coated ants was visible at low magnification (**b** and **c**). However, at high magnification, sample's fine surface structure at

Chapter 1. *In-Situ* TEM Study on Growth Dynamics and Mechanism of Nanobubbles in Graphene Liquid Cells

1.1. Abstract

Dynamics of bubbles is related to various important biological and chemical phenomena. However, the morphology and the growth dynamics of the bubbles at nanoscale have not been fully investigated owing to the lack of proper imaging tools that can visualize nanoscale objects in the liquid phase. Here, we demonstrate for the first time that the nanobubbles in water encapsulated by graphene membrane can be visualized by in-situ ultra-high vacuum transmission electron microscopy. Our microscopic results indicate two distinct growth mechanisms of merging nanobubbles and the existence of a critical radius of nanobubbles that determines the unusually long stability of nanobubbles. Interestingly, the gas transport through ultrathin water membranes at nanobubble interface is free from dissolution, which is clearly different from conventional gas transport that includes condensation, transmission and evaporation.

1.2. Introduction

1.2.1. Internal pressure and life time of bubbles

Formation, evolution and vanishing of bubbles are common phenomena in nature, which can be easily observed in boiling or falling water, carbonated drinks, gas-forming electrochemical reactions, and so on. Creating a bubble is necessary to apply energy required to overcome the effects of surface tension, such as pressure and heat. The surface tension, the energy cost per unit area for generating a new interface of system, is related to the intermolecular interactions that hold surrounding molecules together. It means that the stronger the intermolecular bonding in the materials the bigger the energy cost of creating new surfaces.

If the absence of gravity, the bubble will be in the form of a perfect sphere which has structurally the smallest surface area. It is related to reducing the energy cost of total interfacial area by compressing the gas molecules in the bubble. This pressure inside bubble (ΔP) is described by the

Yong−Laplace equation,

$$\Delta P = 2\gamma/r \quad (1)$$

Where, γ is the interfacial tension of bubble (interface of gas−liquid phase) and r is the radius of the bubble. According to the equation, smaller bubbles have higher internal pressure.

Vapor and gas molecules such as N_2, O_2, H_2, and H_20 can travel from the bubble to the solvent through the bubble's impermeable interface, and *vice versa*. The solubility of these molecules in solvents is determined by the temperature and pressure, and described by the Henry's Law as shown below,

$$C = kP_{gas} \quad (2)$$

Where, C is the solubility of a gas at a fixed temperature in an particular solvent, k is Henry' s law constant, and P_{gas} is the partial pressure of the gas. The internal pressure of bubble is higher than the surrounding liquids and is related to the bubble curvature radius. That is, the smaller the bubbles, the higher the pressure. The high pressure inside the bubble results in an increase in solubility of the gas molecules. The gas moves from the bubble to surroundings by diffusion, which leads to a

decrease in bubble size to keep equilibrium state. Then, this decrease of the radius induces further increase in bubble pressure by the Young–Laplace equation, and more rapid gas diffusion to surroundings. Due to this serial process, small bubbles become shrinking and dissolved in solvent rapidly. According to the theoretical prediction of bubble lifetime for a bubble in water, as a function of starting radius and gas type, the lifetimes of microscale and nanoscale bubbles was ~10^{-1}–10^{-3} s and ~10^{-4}–10^{-6} s, respectively (Fig. 1). Also, Simonsen *et al.* suggested that small contact angle of bubbles effected to the long lifetimes of bubbles. According to their results, the lifetime of the bubbles, having the height of 6.6 nm, contact angle of 11.6° , and a radius of 322 nm, is predicted ~ 1 ms. However, the internal pressure of 5.5 atm is calculated by the Young–Laplace equation, and still much higher than surrounding pressure.

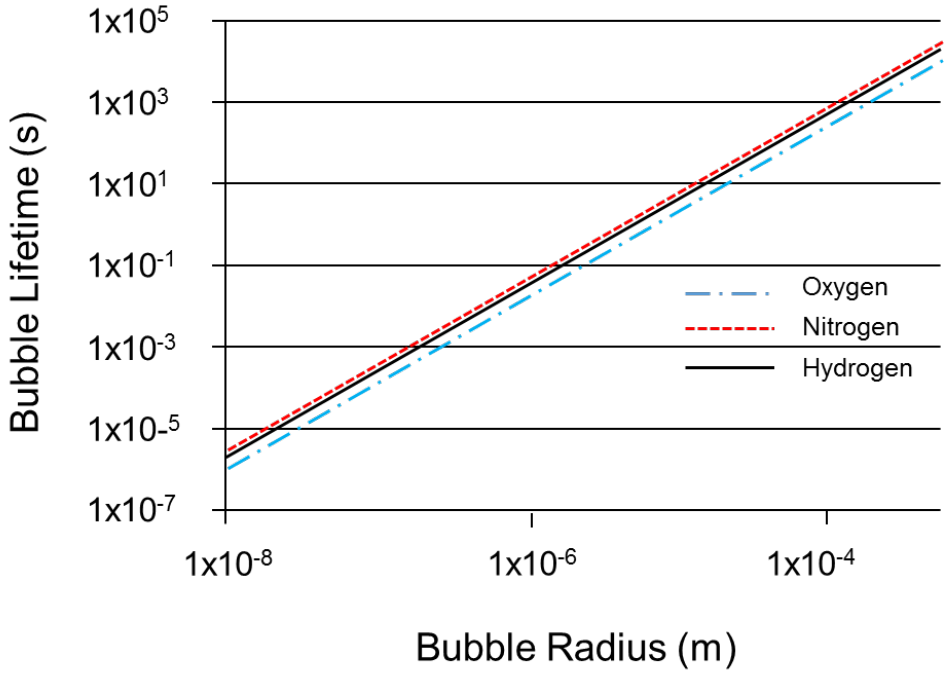

Figure 1. The theoretical predicted bubble lifetime to starting radius and gas type. Diffusion coefficient in water 2 x 10^{-9} m^2/s, Henry's Law coefficient for oxygen 7.9 x 10^4 J/mole, nitrogen 15.6 x 10^4 J/mole, and hydrogen 13 x 10^4 J/mole at 298 K (*Ref.* Craig *et al*, *soft matter* **7**, 40–48 (2011))

1.2.2. Nanoscale bubbles

Above-mentioned, nanoscale bubbles have a very high internal pressure by the Laplace equation. So, it was expected that their lifetime was just too short to be observed by experiments. However, through the many other studies, since the existence of "nanobubbles" was firstly reported by Parker *et al.* in 1994, nanoscale bubbles have been intensively studied. Parker *et al.* found that when the two hydrophobic surfaces immersed in water were brought together, the attractive force clearly increased as a function of distance between the surfaces. They suggested that the presence of nanobubbles on the hydrophobic surfaces acted as a bridge, resulting in increase in the attractive force. Recently, there have been intensive efforts to characterize the nanobubbles in liquid phase, which includes ion conductance measurement through a solid-state nanopore, topographic imaging by atomic force microscopy (AFM) and direct visualization by optical methods. Among them, AFM measurement technique was thought to be the most effective and direct way to provide the morphological information of nanobubbles.

Especially, tapping mode imaging was commonly used to produce a height image of nanobubbles on the hydrophobic surface, while the contact mode of AFM could not provide the correct height images due to the softness of the nanobubbles' interfaces.

Other groups suggested the techniques to prove the existence of nanobubbles and to find out their morphological information by freeze-fractures and rapid cryofixation. In 2011, Uchida *et al.* used a TEM with the freeze-fractured replica method to observe the trapped oxygen micro- and nanobubbles in ice with amorphous state.

None of these, however, is capable of imaging the liquid-phase nanobubbles in real time with sub-10nm resolution. And they can't provide any information about native behaviors such as nucleation, growth, coalescence, and shrinkage of bubbles in real time. In this regard, in-situ transmission electron microscopy (TEM) would be the best method to observe the behaviors of nanobubbles, but the resolution is

still limited by the thickness and the robustness of liquid cell membranes. Recently, it was reported that graphene can be utilized as a perfect liquid cell membrane for in-situ TEM imaging of nanocrystal growth thanks to its atomic thickness, flexibility, extraordinary mechanical strength and high conductivity. Here, we tried to investigate the evolution of nanobubbles by encapsulating them in a graphene liquid cell membrane for in-situ TEM imaging in ultra-high vacuum (UHV-TEM).

1.3. Experimental

1.3.1. Preparation of monolayer graphene

Graphene was synthesized by the chemical vapor deposition (CVD) method on a high-purity copper foil (Alfa Aesar, 99.999%) with flowing 70 mTorr H_2 and 650 mTorr CH_4 gas. As grown graphene on Cu was spin-coated with poly methyl methacrylate (PMMA) and back-side graphene was etched using oxygen plasma. Then, the PMMA layer as a supporting film on graphene was removed by acetone at 50°C for 1 hour. Remaining copper foil was etched in 1.8 wt% ammonium persulfate aqueous solution. Finally, the monolayer graphene was rinsed with distilled water several times to remove the residual metal ions and salts.

1.3.2. HRTEM observation of nanobubbles

Electron microscopic analysis was carried out using *in-situ* UHV-TEM (JEOL, JEM 2010V) operated at an accelerating voltage of 200 keV. Its point resolution at Scherzer defocus is 0.23 nm and lattice resolution is 0.20 nm.

The ultimate base pressure in the chamber was less than $2x10^{-10}$ Torr, and the pressure during observation was below $5x10^{-9}$ Torr. All the experiments shown here were performed at room temperature. The UHV *in-situ* high-resolution TEM (HRTEM) observations were employed optimized parameters for imaging, that is, there were recorded close to the Scherzer defocus and the sample height was adjusted to keep the objects focused in the optimum lens current, because HRTEM images often change depending on the high beam current density and defocus. *In-situ* real-time HRTEM images were recorded by a digital video recorder at the time resolution of 1/30 s equipped with an online TV camera system (Gatan model 622SC).

A typical electron beam current density at the specimens was a very small value of ~1 Acm^{-2}. It is well known that an electron beam can adversely affect irradiation damages of a sample during examination in an electron microscope (EM; for example, heating, electrostatic charging, ionization damage, displacement damage, sputtering and

hydrocarbon contamination). However, the above-mentioned observation conditions, especially a very small current density and an UHV situation reduced the risk of irradiation damages and hydrocarbon contaminations to the minimum. Although atomic resolution of the JEM 2010V with a LaB6 filament used in this study as compared with that of an EM with a field-emission gun filament falls, its current density is lower by about 100–1,000 times than that of the field-emission gun filament. Moreover, the current density of ~1 Acm^{-2} at most brings a temperature increase of a few degrees of Celsius, which perhaps hardly influences the sample in a recoding time, usually 2–5 min. In fact, while observing the magnified images, no changes in image detail arising from electron beam irradiations were detected. Therefore, we believed that these advantages as well as unique capabilities of graphene liquid cell as a perfect membrane for EM imaging has enabled the characterization of nanobubbles without contamination in this study.

1.4. Results and Discussion

1.4.1. Characterization of graphene liquid cells

The graphene liquid cell was fabricated by the sequential wet transfer of monolayer graphene synthesized by chemical vapor deposition (Fig. 2). To fabricate a graphene coated TEM grid, the monolayer graphene without PMMA support was prepared by removing PMMA with acetone, followed by Cu etching with 1.8 wt% ammonium persulfate (APS) solution. Finally rinsing and transferring complete the graphene-supported TEM grid. The water islands are naturally captured during the wet transfer process of graphene to a graphene-supported TEM grid, where residual water on graphene can be trapped naturally between two graphene layers. The quality of graphene-supported TEM grids are verified by a high-resolution imaging transmission electron microscope (HR-TEM) and a high-angle annular dark field (HAADF) scanning transmission electron microscope (STEM) (Fig. 3). The monolayer graphene without supporting film is well-covered on the Cu grid, where

the critical defects are not observed at the nano- and atomic-resolution images.

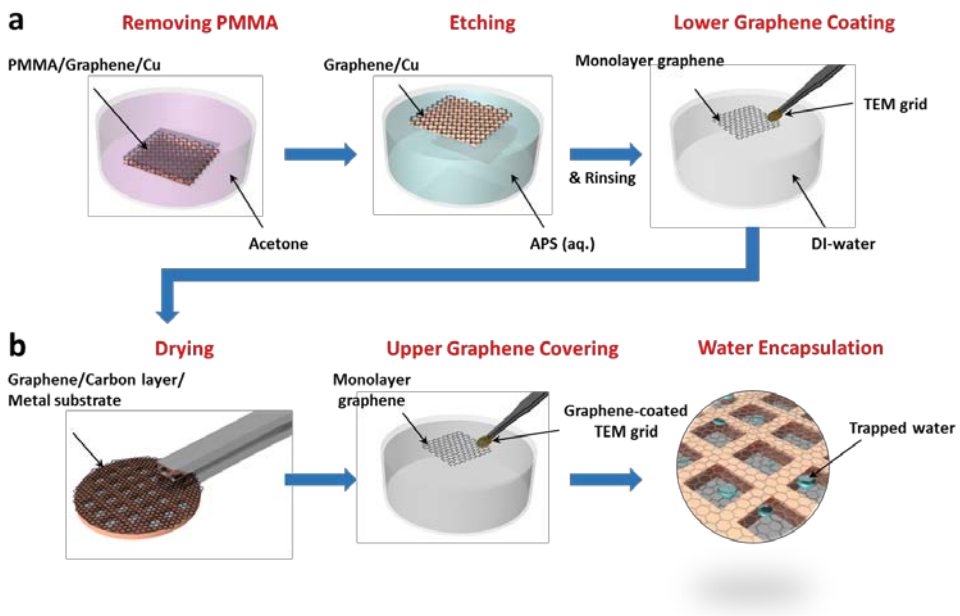

Figure 2. Schematic representation for the preparation processes of graphene liquid cells. a, Fabrication of graphene coated TEM grid. b, Capturing water islands by transferring the second layer graphene. After drying, another monolayer graphene floating on water was transferred on to the graphene-supported TEM grid, where residual water on graphene can be trapped naturally between two graphene layers.

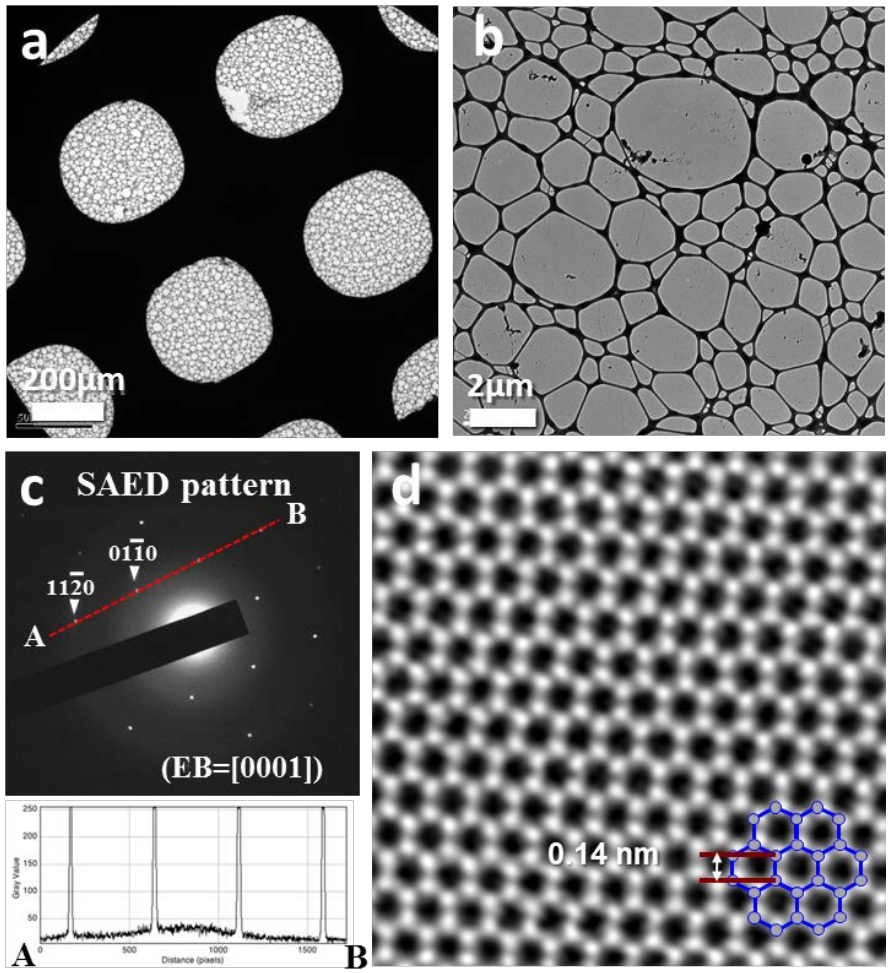

Figure 3. Characterization of high quality CVD graphene using HR-TEM and HAADF-STEM. a and b, TEM images of monolayer graphene on a Cu grid with amorphous carbon as support layer. c, Selected area electron diffraction (SAED) pattern of graphene monolayer, evidenced by the same intensity along the A-B line profile. d, Atomic resolution image of high quality graphene obtained by HAADF-STEM.

1.4.2. Observation of nanobubbles

As shown in Figs. 4 and 5, the top and side views of nanobubbles show the plano-convex morphology whose diameter ranges from 5 to 15 nm, respectively. It should be noted that the high mechanical flexibility and strength of graphene allows the cross-sectional imaging of nanobubbles in a folded (or cut) liquid cell (Fig. 6). Even though the image resolution in side views is not high enough to confirm the exact shapes of all the nanobubbles, the majority of the observed bubbles shows a plano-convex shape whose contact angle varies from 60 to 90° (Figs. 5, 7, and 8). This range of contact angles was used to calculate the internal pressure of nanobubbles using the Young-Laplace equation, $\Delta P = 2\gamma / R_c$, where ΔP is the pressure difference across the nanobubble interface, γ is the surface tension of water, and R_c is the curvature radius of nanobubbles (Fig. 9). For example, Young-Laplace pressure inside a 10-nm-diameter nanobubble, which has a contact angle of 72°, is calculated to be 27 MPa, which is 270 times higher than ambient pressure.

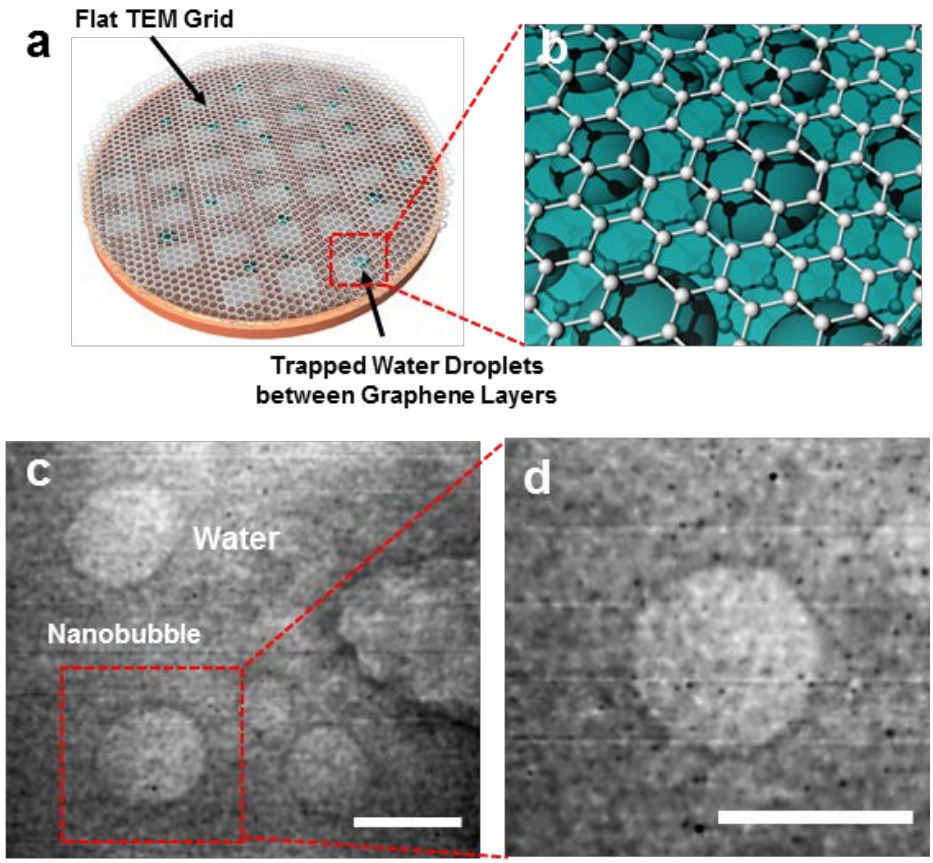

Figure 4. Morphology of nanobubbles in graphene liquid cell. (a–d) A graphene liquid cell fabricated on a flat TEM grid (copper or molybdenum) showing the top views of nanobubbles. (c and d) *In-situ* snapshot images of nanobubbles obtained by ultra-high vacuum (UHV) TEM (200 keV, ~$5x10^{-9}$ Torr). Scale bars, 10 nm.

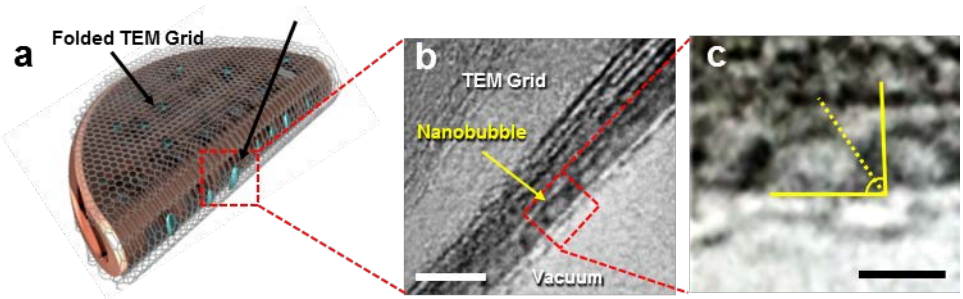

Figure 5. Morphology of nanobubbles in graphene liquid cell.

(a–c) A folded graphene liquid cell showing the side views of nanobubbles. The contact angles were roughly measured to be 60°–90°. Scale bars for f and g, 10 and 5 nm, respectively.

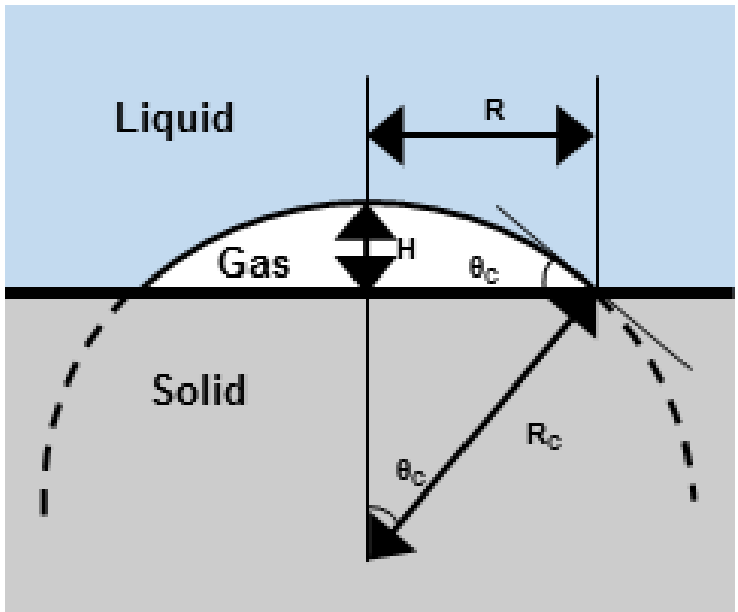

Figure 6. A schematic image of a nanobubble on solid surface and its structural parameters including surface radius (R), contact angle (θ_c), curvature radius (R_c) and height (H).

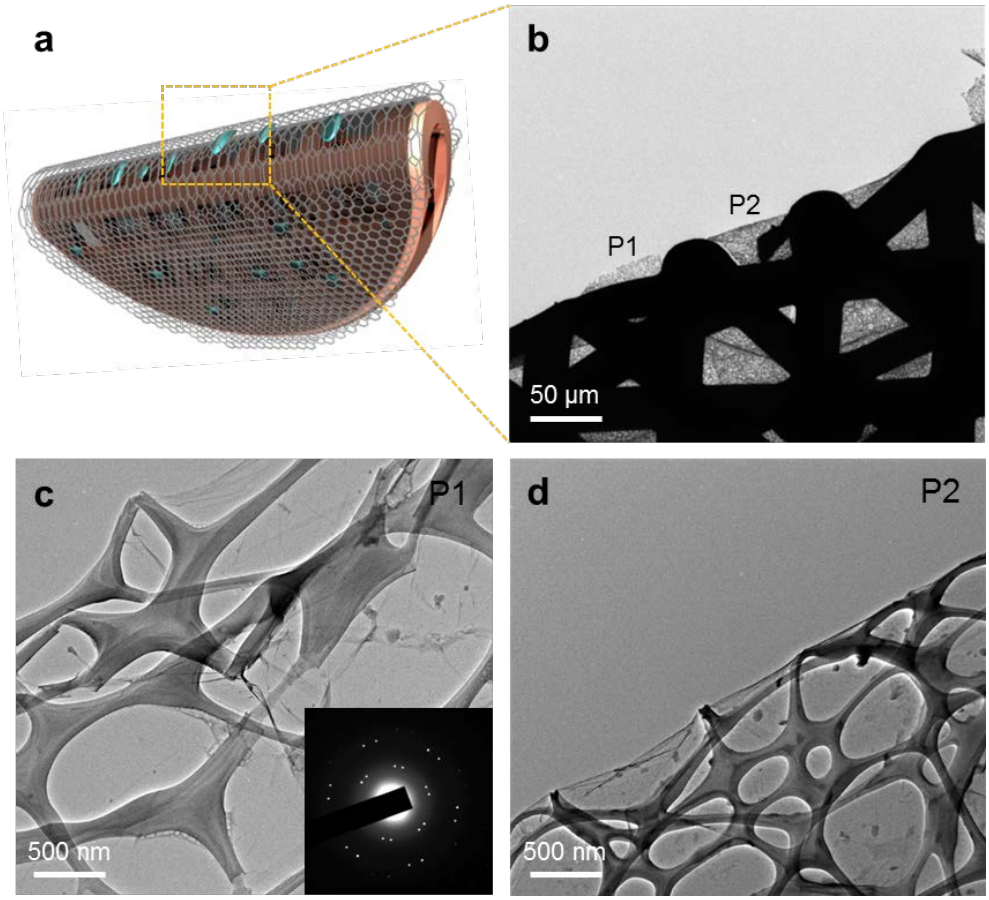

Figure 7. Morphology of folded graphene liquid cells on a TEM grid. a, Schematic illustration of folded graphene liquid cell on a TEM grid. **b–d**, Low and high magnification TEM images of the folded graphene liquid cells. The P1 and P2 indicate the cut and folded parts of graphene liquid cells, respectively. The inset image in C shows the selected area electron diffraction (SAED) pattern of two overlapping graphene monolayers.

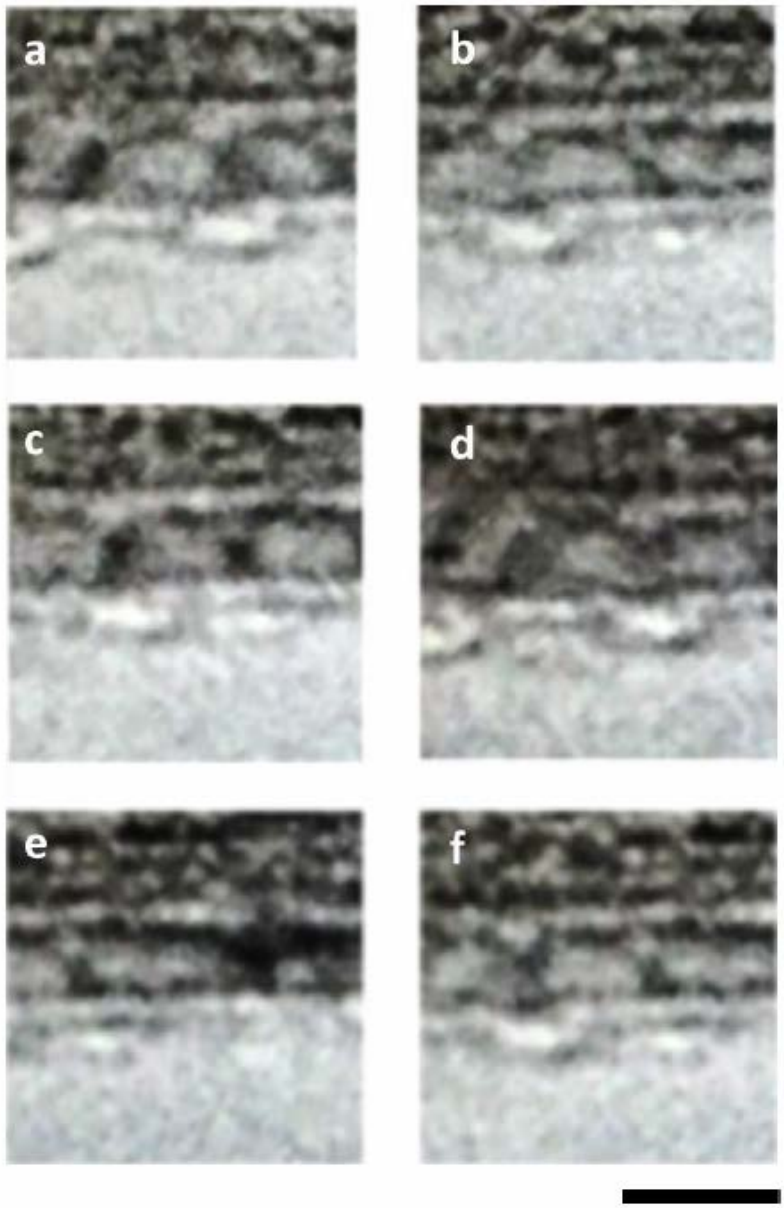

Figure 8. Cross-sectional TEM images of nanobubbles in a graphene liquid cell. a-f, TEM images showing the side view of various nanobubbles in water trapped between sandwiched graphene. Scale bar, 5 nm.

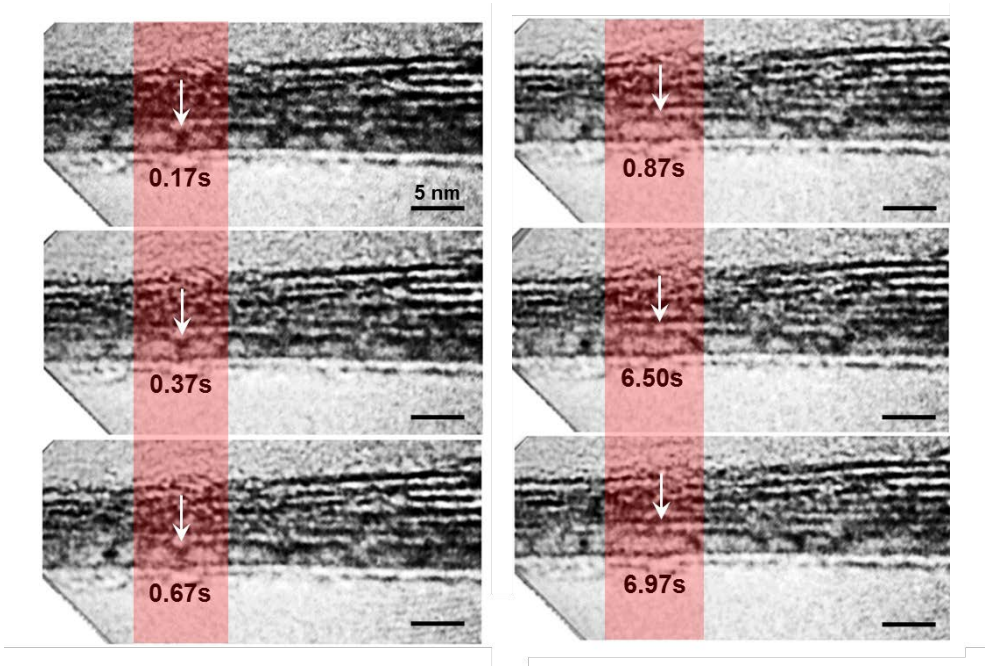

Figure 9. Snap shots of TEM movies showing the side views of nanobubbles. The white arrows indicate the two coalescing nanobubbles. Scale bars, 5 nm.

1.4.3. Stability of nanobubble

According to classical diffusion theory, the lifetime of a nanobubble was predicted to be ~1 ms. In fact, however, nanobubbles are very stable even for several hours as revealed by liquid–phase AFM. Many explanations on this superstability of nanobubbles were proposed, including stabilization by three–phase contact line pinning and dynamic equilibrium at water–vapor interface. In addition, the critical radius of stable nanobubbles was predicted to be ~1.7 nm by molecular dynamic simulation and ~85 nm by dynamic equilibrium theory, but there has been no experimental confirmation so far. Here we show, for the first time, that the critical radius of stable nanobubbles is 6.3±0.8 nm as shown in Fig. 10a,b. For the nanobubble radius below the critical radius, the radius keeps decreasing until it completely collapses, whereas the nanobubble lager than 6.3±0.8 nm persists for more than 10 min.

In addition, the stable radius of nanobubbles are calculated considering the structural parameters from TEM

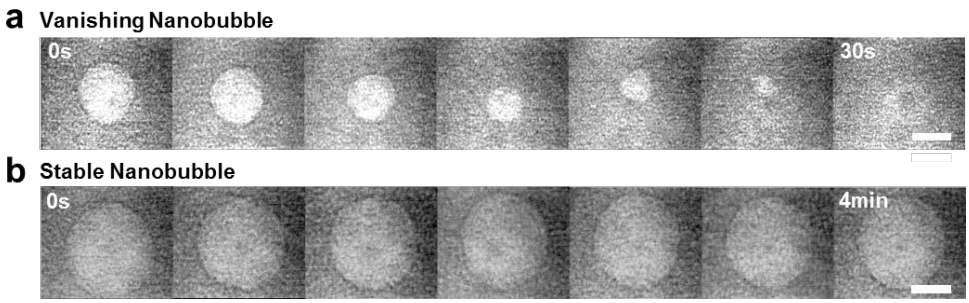

Figure 10. (a and b) The snap shots of TEM images showing the vanishing and stable nanobubbles, respectively. The nanobubbles smaller than critical radius tend to shrink with time and disappear in ~40 s, whereas the larger bubbles persist for more than 10 min. Scale bars, 5 nm.

observation and the molecular dynamics (MD) simulation results by Matsumoto *et al.*. The setting temperature of water is 300K, and the system volume is fixed at V = 30 x 30 x 7.5 $(nm)^3$. The liquid pressure of system P_{sys} can be estimated from the density of liquid ρ_{liq} as,

$$P_{sys} = A\,\frac{mN}{V - V_{bubble}} + B \qquad (3)$$

where m is the molecular mass of water, N is the number of molecules, and $V_{bubbule}$ is the volume of nanobubble. A and B are the constants determined approximately by a linear function of P_{sys} with respect to ρ_{liq}. Considering the plano–convex shape of nanobubbles, $V_{bubbule}$ was calculated by simple integral as

$$V_{bubble} = \int_{R_c - H}^{R_c} \left({R_c}^2 - y^2\right)\pi dy = \pi R^3 \left\{ \frac{\left(\tan\frac{\theta_c}{2}\right)^2}{\sin\theta_c} - \frac{1}{3}\left(\tan\frac{\theta_c}{2}\right)^3 \right\} \qquad (4)$$

The surrounding liquid pressure of nanobubble, P_{liq} is given by $P_{liq} = P_{vap} - \Delta P$, where P_{vap} is the gas pressure inside the nanobubble and ΔP is Young–Laplace pressure. At 300 K, the vapor density inside nanobubble is very low, so it can be set as $P_{vap} = 0$ in our calculation. Thus, P_{liq} simply can be expressed as $\sim -\Delta P$. Now the radius of stable nanobubble can

be derived from the equilibrium equation between liquid and system pressure, $P_{liq} = P_{sys}$ as following:

$$-\frac{2\gamma \sin\theta_C}{R} = \frac{AmN}{6750 - \pi R^3 \left\{ \frac{\left(\tan\frac{\theta_C}{2}\right)}{(\sin\theta_C)^2} - \frac{1}{3}\left(\tan\frac{\theta_C}{2}\right)^3 \right\}} + B \qquad (5)$$

The constant values are approximated as A = 2 x 10^{24}, B = − 1980, γ = 71.97 mN m^{-1} and N = 211,003. A and B are adopted from the MD simulation by Matsumoto *et al.*, θ_c is roughly measured to be 60~90° based on the TEM results, and γ is the surface tension of water. In this way, the stable radius of a nanobubble are calculated to be 5.04~5.21 nm, which falls into the critical radii range of vanishing and stable nanobubbles in Fig. 10a,b, even though the attraction between the gas molecule and graphene surface can be neglected in our model. Figure 11 and 12 show that there exists critical radius range for the stability of nanobubbles. The nanobubbles whose radii larger than 6 nm persist more than 10 min, whereas smaller bubbles tend to disappear in 1 min.

This result is complementary to those established by the Water−ethanol exchange route and AFM. The key differences

include that (i) the lateral size of nanobubbles examined by AFM is significantly larger than that shown here, and (ii) the stabilization mechanisms are different. In the AFM studies, it has recently been shown that the interfacial gas enrichment (IGE; interfacial dense gas layer) is the key stabilization mechanism. The nanobubbles observed here can be stabilized by the mechanism described by the balance between diffusion and attraction of gas molecules to the graphene surface. As our nanobubbles have been prepared by the wet transfer process, the gas concentration at the surface may not be sufficient high to form an IGE, whereas in the water–ethanol exchange the gas concentration at the surface is high and an IGE can be formed. The driving force of the IGE formation is also the attraction between the gas molecules and the solid surface. These different stabilization mechanisms also lead to difference in the contact angles obtained by AFM (~150°) and in here (60–90°).

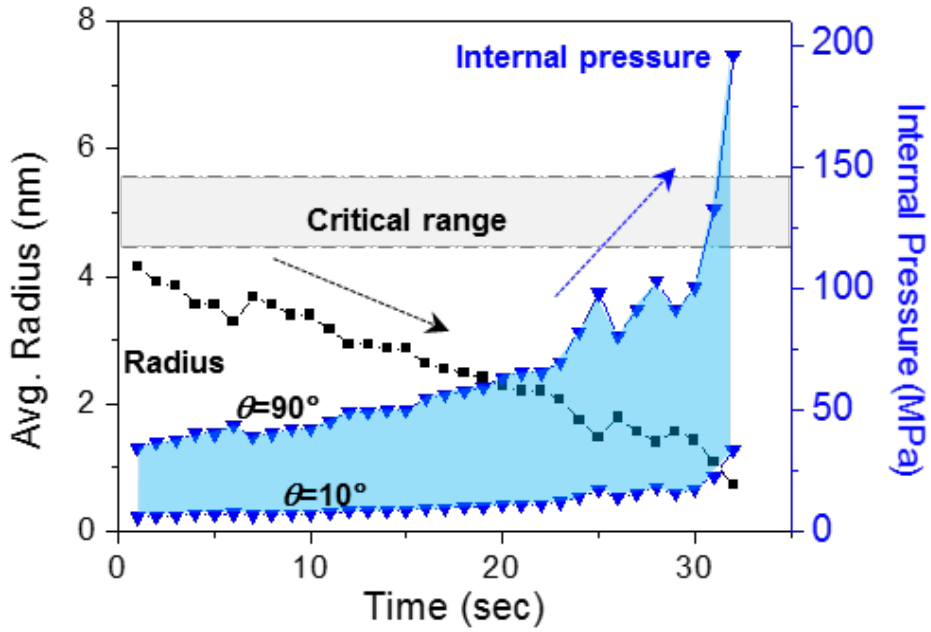

Figure 11. Average (Avg.) radius and internal pressure changes of vanishing single nanobubbles with time. The pressure was calculated by Young–Laplace equation. The grey shaded area presents the critical radius range based on TEM observation. The blue shaded area presents the internal pressure range depending on varying contact angles (θ).

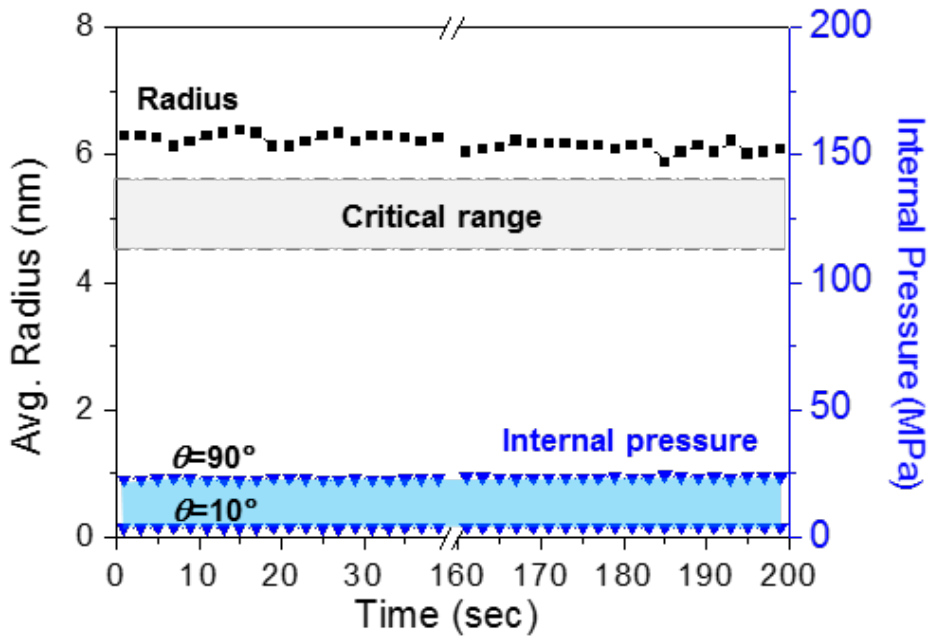

Figure 12. Average (Avg.) radius and internal pressure changes of stable single nanobubbles with time. The grey shaded area presents the critical radius range based on TEM observation. The blue shaded area presents the internal pressure range depending on varying contact angles (θ).

1.4.4. Growth of nanobubbles

Nanobubbles are growing by merging with adjacent nanobubbles, which shows clearly different two pathways depending on their relative sizes. In case that the sizes are distinctively different (R>R′), the smaller bubble tends to disappear near the surface of the growing larger bubble (Fig. 13a), which is similar to Ostwald ripening that is known as a solid-state phenomenon that small crystals are dissolved and redeposited onto the surface of larger crystals. It seems that gas diffuses from one bubble to another across the persisting boundary. On the other hand, two similar-sized nanobubbles (R≈R′) show a coalescing process after breaking their interface, followed by reshaping into dumbbell-like and spherical morphology (Fig. 13b).

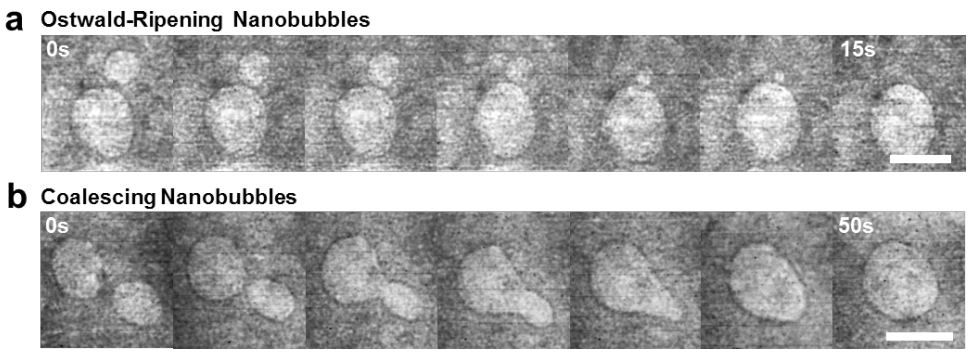

Figure 13. (a and b) The snap shots of TEM images showing the merging of adjacent two nanobubbles observed for 15 and 50 s, respectively. When the nanobubble sizes are significantly different, it shows an Ostwald ripening-like merging process, whereas the similar-sized bubbles are coalescing as their inter-bubble boundary breaks. Scale bars, 10 nm.

1.4.5. Gas transport between nanobubbles

In the Ostwald ripening-like process, the radius of the smaller nanobubble shows a change in slope with respect to time, whereas the radius of the larger bubble steadily increases (Figs. 14 and 15). Here, we suppose that a new pathway of gas diffusion is created when the thickness of the interface is smaller than ~2.3 nm, where the instantaneous rupture of the interface allows the massive diffusion from a highly pressurized smaller bubble to a larger bubble. We define it as 'direct gas diffusion (or transport)' to be distinguished from 'indirect gas diffusion'. The internal pressure of the small nanobubble increases from 140 to 400 MPa for the contact angle of 72° as shown in Fig. 13b, which is driving force for gas transport from the small bubble to the large bubble.

Figure 16 shows the two different pathways of gas transport (Fig. 16a) and time-resolved TEM section analysis of Ostwald ripening nanobubbles (Fig. 16b). Usually, conventional gas transport between remote nanobubbles

includes condensation, transmission and evaporation steps. However, in case that two Ostwald ripening nanobubbles come into contact with each other, the gaseous particles seem to diffuse as a discrete packet from one to another through the ultrathin water membrane without hydration, which needs to be importantly considered for the assembly and function of biomolecules and other systems where nanoscale gas state is involved. The instantaneous breakjunction of the ultrathin water membrane appears dominantly as the thickness decrease below ~2 nm as shown in Fig. 16b.

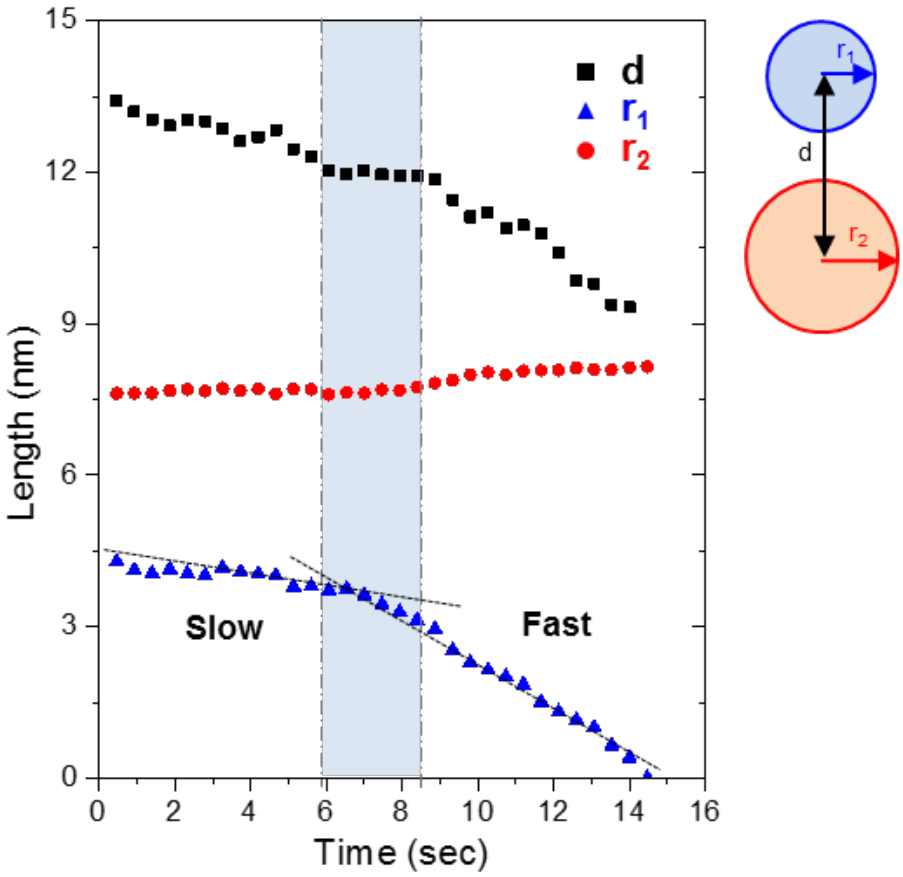

Figure 14. Analysis of Ostwald ripening nanobubbles. Time evolution of radius of growing (red), vanishing (blue) nanobubble and inter-bubble distance measured in Fig. 10a.

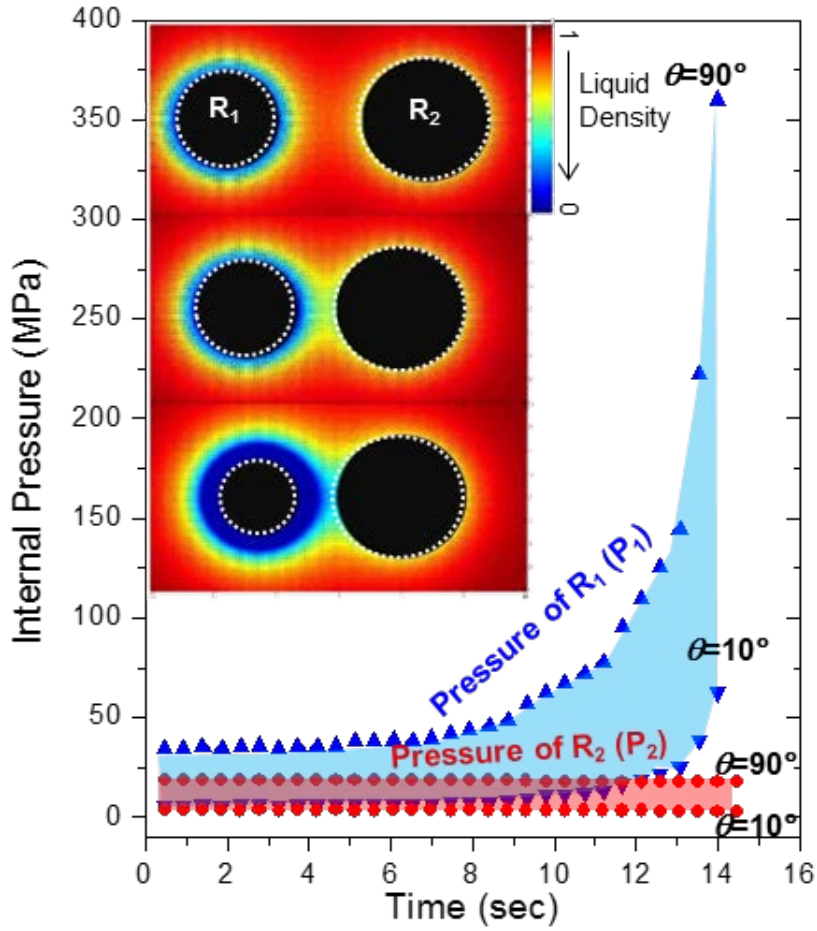

Figure 15. Calculated internal pressure range of Ostwald ripening nanobubbles in Fig. 10a. The inset shows the calculation result representing the liquid water density with respect to their relative size and distance between two adjacent nanobubbles, indicating that the water density decreases at the interface region as two bubbles get closer, which is a driving force to put two remote bubbles together.

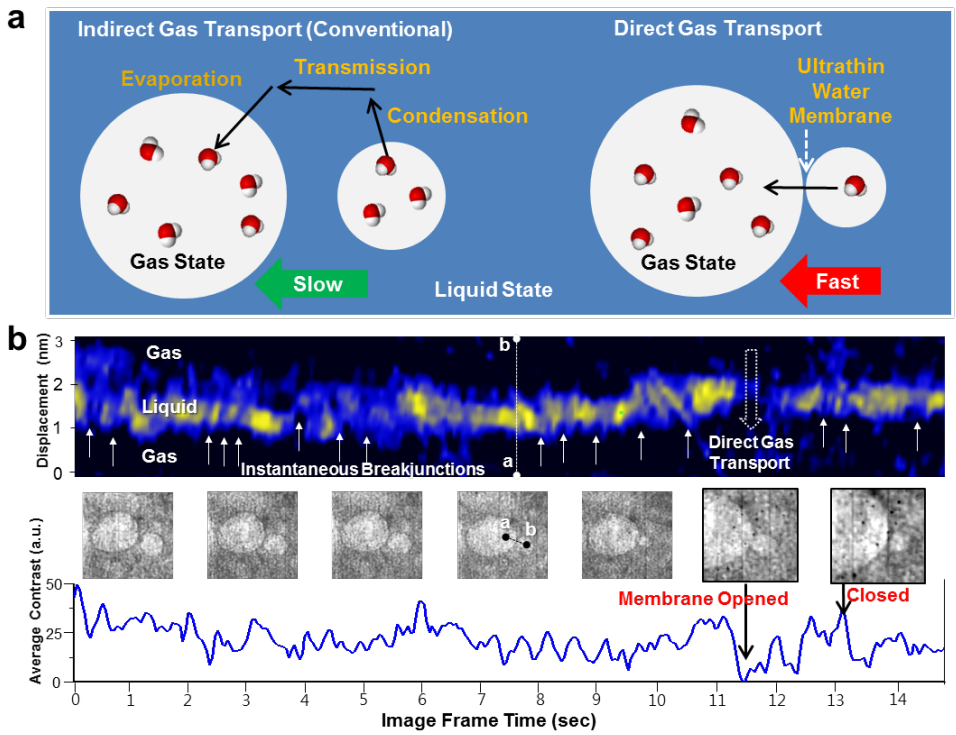

Figure 16. Direct and indirect gas transport in Ostwald ripening nanobubbles. (a) Schematic representations explaining indirect and direct gas transport. Between two remote nanobubbles, gases are slowly transported through conventional condensation, transmission and evaporation processes, whereas interfacial nanobubbles show direct gas transport through the ultrathin water membrane without hydration. (b) Time-resolved TEM section analysis of the inter-bubble region (line A-B), extracted from a Movie related to Fig. 13a. The thickness of water layer gradually decreases with time, and the occurrences of instantaneous

breakjunctions are clearly observed as indicated by white arrows. Opening and closing of water membrane are clearly visible between 11 and 13 s.

1.5. Conclusion

The liquid-phase nanobubbles encapsulated by graphene membrane were visualized by in-situ UHV-TEM, showing the critical radius of nanobubbles determining its long-term stability as well as two different growth processes of merging nanobubbles depending on their relative sizes. It is remarkable that the instantaneous rupture of the ultrathin water membrane between nanobubbles allows direct unhydrated gas transport that has not been observed so far. We believed that this phenomenon needs to be importantly considered in various biological and environmental systems where nanoscale gas state is involved. Other two dimensional materials such as boron nitride (BN) or molybdenum disulfide (MoS_2) are also expected to be useful for the preparation of graphene liquid cells because there might be different behaviours of nanobubbles depending on varying surface hydrophobicity or mechanical flexibility.

If additionally mentioned, the exact three-dimensional

shape of nanobubble has not been verified experimentally until now. To understand the physical property and the evolution behaviour of nanobubble exactly, it is needed to conduct more in depth study on the side view of nanobubble as a future work.

1.6. References

1. Arielia, R. & Marmurb, A. Decompression sickness bubbles: are gas micronuclei formed on a flat hydrophobic surface? *Respir. Physiol. Neurobiol.* **177**, 19-23 (2011).
2. Nakabayashi, S., Shinozaki, R., Senda, Y. & Yoshikawa, H. Y. Hydrogen nanobubble at normal hydrogen electrode. *J. Phys. Condens. Matter* **25**, 184008 (2013).
3. Ishida, N., Inoue, T., Muyahara, M. & Higashitani, K. Nano bubbles on a hydrophobic surface in water observed by tapping-mode atomic force microscopy. *Langmuir* **16**, 6377-6380 (2000).
4. Ishida, N. Direct measurement of hydrophobic particle-bubble interactions in aqueous solutions by atomic force microscopy: effect of particle hydrophobicity. *Colloids Surf. A Physicochem. Eng. Asp.* **300**, 293-299 (2007).
5. Koishi, T. et al. Nanoscale hydrophobic interaction and nanobubble nucleation. *Phys. Rev. Lett.* **93**, 185701 (2004).
6. Zhang, X., Khan, A. & Ducker, W. A Nanoscale gas state. *Phys. Rev. Lett.* **98**, 136101 (2007).

7. Nam, Y. & Ju, Y. S. Bubble nucleation on hydrophobic islands provides evidence to anomalously high contact angles of nanobubbles. *Appl. Phys. Lett.* **93**, 103115 (2008).
8. Simonsen, A. C., Hansen, P. L. & Klosgen, B. Nanobubbles give evidence of incomplete wetting at a hydrophobic interface. *J. Colloid Interface Sci.* **273**, 291-299 (2004).
9. Stevenson, P. Inter-bubble gas diffusion in liquid foam. *Curr. Opin. Colloid Interface Sci.* **15**, 374-381 (2010).
10. Tyrrell, J. W. G. & Attard, P. Images of nanobubbles on hydrophobic surfaces and their interactions. *Phys. Rev. Lett.* **87**, 176104 (2001).
11. Smeets, R., Keyser, U., Wu, M., Dekker, N. & Dekker, C. Nanobubbles in solidstate nanopores. *Phys. Rev. Lett.* **97**, 088101 (2006).
12. Hampton, M. A. & Nguyen, A. V. Nanobubbles and the nanobubble bridging capillary force. *Adv. Colloid Interface Sci.* **154**, 30-55 (2010).
13. Karpitschka, S. et al. Nonintrusive optical visualization of surface nanobubbles. *Phys. Rev. Lett.* **109**, 066102 (2012).
14. Chan, C. U. & Ohl, C.-D. Total-internal-reflection-

fluorescence microscopy for the study of nanobubble dynamics. *Phys. Rev. Lett.* **109**, 174501 (2012).

15. Mishima, T. D., Naruse, N., Cho, S.-P., Kadohira, T. & Osaka, T. Direct imaging of the InSb(001)-c(8□2) surface: evidence for large anisotropy of the reconstruction. *Phys. Rev. Lett.* **89**, 276105 (2002).

16. Cho, S.-P., Nakamura, J., Tanaka, N. & Osaka, T. Direct observation of Au deposition processes on InSb{111}A,B - (2 x 2) surfaces. *Nanotechnology* **15**, S393-S397 (2004).

17. Yuk, J. M. et al. High-resolution EM of colloidal nanocrystal growth using graphene liquid cells. *Science* **336**, 61-64 (2012).

18. Kim, K. S. et al. Large-scale pattern growth of graphene films for stretchable transparent electrodes. *Nature* **457**, 706-710 (2009).

19. Li, X. et al. Large-area synthesis of high-quality and uniform graphene films on copper foils. *Science* **324**, 1312-1314 (2009).

20. Bae, S. et al. Roll-to-roll production of 30-inch graphene films for transparent electrodes. *Nat. Nanotech.* **4**, 574-578

(2010).

21. Stig Ljunggren, S. & Eriksson, J. C. The lifetime of a colloid–sized gas bubble in water and the cause of the hydrophobic attraction. *Colloids Surf. A* **130**, 151-155 (1997).

22. Borkent, B., Dammer, S., Scho ¨ nherr, H., Vancso, G. & Lohse, D. Superstability of surface nanobubbles. *Phys. Rev. Lett.* **98**, 204502 (2007).

23. Weijs, J. H. & Lohse, D. Why surface nanobubbles live for hours. *Phys. Rev. Lett.* **110**, 054501 (2013).

24. Seddon, J. R. T., Zandvliet, H. J. W. & Lohse, D. Knudsen gas provides nanobubble stability. *Phys. Rev. Lett.* **107**, 116101 (2011).

25. Brenner, M. & Lohse, D. Dynamic equilibrium mechanism for surface nanobubble stabilization. *Phys. Rev. Lett.* **101**, 214505 (2008).

26. Matsumoto, M. Surface tension and stability of a nanobubble in water: molecular simulation. *J. Fluid Sci. Tech.* **3**, 922-929 (2008).

27. Peng, H., Hampton, M. A. & Nguyen, A. V. Nanobubbles do

not sit alone at the solid–liquid surface. *Langmuir* **29**, 6123 (2013).

28. Peng, H., Birkett, G. R. & Nguyen, A. V. Origin of interfacial nanoscopic gaseous domains and formation of dense gas layer at hydrophobic solid–water interface. *Langmuir* **29**, 15266 (2013).

29. Lee, J., Laoui, T. & Karnik, R. Nanofluidic transport governed by the liquid/vapour interface. *Nat. Nanotech.* **9**, 317-323 (2014).

30. Egerton, R. F., Li, P. & Malac, M. Radiation damage in TEM and SEM. *Micron* **35**, 399-409 (2004).

31. Pantelic, R. S., Meyer, J. C., Kaiser, U. & Stahlberg, H. The application of graphene as a sample support in transmission electron microscopy. *Solid State Commun.* **152**, 1375-1382 (2012).

Chapter 2. Non-Destructive SEM Imaging and Analysis of Biological Samples with Graphene Coating

2.1. Abstract

In electron microscopy, charging of non-conductive biological samples by focused electron beams hinders their high-resolution imaging. Gold or platinum coatings have been commonly used to prevent such sample charging, but it disables further quantitative and qualitative chemical analyses by energy dispersive spectroscopy (EDS). Here we report that graphene-coating on biological samples enables nondestructive high-resolution imaging by scanning electron microscopy (SEM) as well as chemical analysis by EDS, utilizing graphene's transparency to electron beams, high conductivity, outstanding mechanical strength, and flexibility. We believe that the graphene-coated imaging and analysis would provide us a new opportunity to explore various biological phenomena unseen before due to the limitation in sample preparation and image resolution, which will broaden our understanding on the life mechanism of various living organisms.

3.1. Introduction

Comprehensive understanding of biological objects - their chemical, physiochemical and biological characteristics - can be effectively achieved through electron microscopy (EM) analysis, preferably without any fixation or auxiliary surface treatment. Scanning electron microscope (SEM) and transmission electron microscope (TEM) are increasingly more employed as they provide direct imaging of specimen's morphological structures with high-resolution. Recently, EM analysis has extended its use to construct three-dimensional structure of the biological specimen with combination of serial block-face sectioning or focused ion beam. In addition, the unique interaction between electron beams and specimen enables various physical and chemical analyses such as energy dispersive spectroscopy (EDS), electron probe micro analysis (EPMA), and electron energy loss spectroscopy (EELS). Nevertheless, charge accumulation on non-conductive surface by electron beams has always hindered EM-mediated biological studies as it distorts the

morphological and chemical characteristics of the specimens. Thus, various metal deposition methods have been employed to dissipate the charge in the non-conducting specimens. However, the relatively thick metal coatings hamper from studying sample's fine surface structure at nanometer scale, because the surface features smaller than metal grain size (~10 nm) cannot be imaged properly. In addition, X-ray fluorescence signals required for EDS analysis are screened by metal layers. Furthermore, it is usually difficult to use the metal-coated samples for further analyses such as TEM that requires electron transparency.

Here we report that graphene-coating on biological samples enables nondestructive high-resolution imaging by scanning electron microscopy (SEM) as well as chemical analysis by EDS, utilizing graphene's transparency to electron beams, high conductivity, outstanding mechanical strength, and flexibility. We believe that the graphene-coated imaging and analysis would provide us a new opportunity to explore various biological phenomena unseen before due to

the limitation in sample preparation and image resolution, which will broaden our understanding on the life mechanism of various living organisms.

A recent progresses in large scale synthesis of high quality graphene films using chemical vapor deposition (CVD) methods have widened its potential in practical device applications as well as unique interests in basic scientific researches. The feasibility of the large scale fabrication of continuous graphene films as well as easy transfer onto diverse biological objects opens up a unique opportunity to create new hetero-interfaces or interfaces with non-conducing biological samples. As demonstrated in a recent work, the in-situ high-resolution EM imaging of nanocrystal growth has been achieved by using graphene liquid cells to encapsulate nanoscale materials as well as their environment (i.e. liquid) and separate them from the vacuum environment. In this regard, graphene mediated coating on biological samples can provide high-resolution EM imaging and chemical analysis due to the excellent electron and heat flow thorough

the graphene and electron-transparency. Here, with taking all these advantages of graphene films, we have employed continuous graphene films as coating for biological samples and exploited them for non-destructive high-resolution electron microscopy imaging and chemical analysis.

2.3. Experimental

2.3.1. Preparation of monolayer graphene

Monolayer graphene was synthesized by chemical vapor deposition method on a high purity copper foil (Alfa Aesar, 99.999 %). The flows of H_2 and CH_4 were 70 and 650 mTorr, respectively. Poly(methyl methacrylate) (PMMA) was spin-coated on the as grown graphene as a support. Unnecessary back-side graphene was etched by using O_2 plasma. Before final use, the PMMA film was removed by hot acetone. The remaining copper foil was etched in 1.8 wt% ammonium persulfate (APS) solution, followed by rinsing with distilled water (DI-water) several times.

2.3.2. Electron microscopy of biological samples

Electron microscopic imaging and chemical analysis were carried out using field-emission scanning electron microscope (FE-SEM, Carl Zeiss, SUPRA 55VP) equipped with an EDS system that operates at 2 to 20 keV. The resolution limit is 1.0 nm at 15 keV and 1.7 nm at 1 kV,

respectively. The pressure in the chamber during observation was less than 10−5 mbar. All the experiments were carried out at room temperature. The sputter coater (BAL−TEC, SCD 005) was used for preparation of Pt−coated samples under argon atmosphere. The applied current and working pressure of the chamber were around 20 mA and 5×10^{-2} mbar, respectively. The sputtering time was 150 seconds, and the work distance was 50 mm for 10 nm−thick Pt−coating.

2.3.3. Preparation of water fleas fed on cerium oxide nanoparticles

The water fleas, Daphnia pulex, were purchased from Green Fish Mall. The ~25 nm CeO_2 nanoparticles were purchased from Sigma−Aldrich and dispersed in a natural water with 5 mg/100 ml concentration. One day after putting in 50 ml CeO_2 solution, the water fleas were rinsed for a few minutes to remove residual salts and CeO_2 nanoparticles, followed by natural drying.

2.3.4. Monte Carlo simulation by CASINO software

To confirm the possibility of graphene sheet as a membrane for electron microscopy of non-conducting biological objects, CASINO v.2.48, a modelling software based on Monte Carlo simulation, was used in this work (http://www.gel.usherbrooke.ca/casino/). The graphene layer was configured as 1 nm thick carbon layer. Chitin was configured as a 10,000 nm thick layer consisted of C, O, N, and H with ratios of 0.4, 0.25, 0.05, and 0.3, respectively. The number of electrons to simulation and displayed trajectories were 100,000 and 2,000, respectively. As a physics model, the Mott by interpolation was selected in a total cross section and a partial cross section. The Casnati model was selected in effective section ionization, and the model by Joy and Luo (1989) was selected in an ionization potential. The Press model was chosen as a random number generator, and the Drouin's model (1996) was selected as a directing parameter.

2.4. Results and Discussion

2.4.1. Comparison between graphene and conventional coating

As schematically displayed in Fig. 17, the unique feasibility and availability of continuous graphene films at large scale enables the conformal coating of biological objects including leaves, ants, spiders, neuron cells, and *Escherichia coli* (*E. coli*), whose sizes range from several centimeters down to few micrometers. Atomically-thin and electrically-conducting graphene membranes were prepared on non-conducting biological surface by isolating graphene films from copper (Cu) foils after CVD growth, followed by conformal coating onto biological samples as illustrated in Fig. 17c. Compared to other conventional sample preparation methods including fixation and metal sputter coating (Figs. 17a and 17b), the present method based on graphene coating is relatively simple, bio-friendly, and non-destructive, which is particularly advantageous for preserving samples for further experiments. Monolayer graphene film was prepared on high-

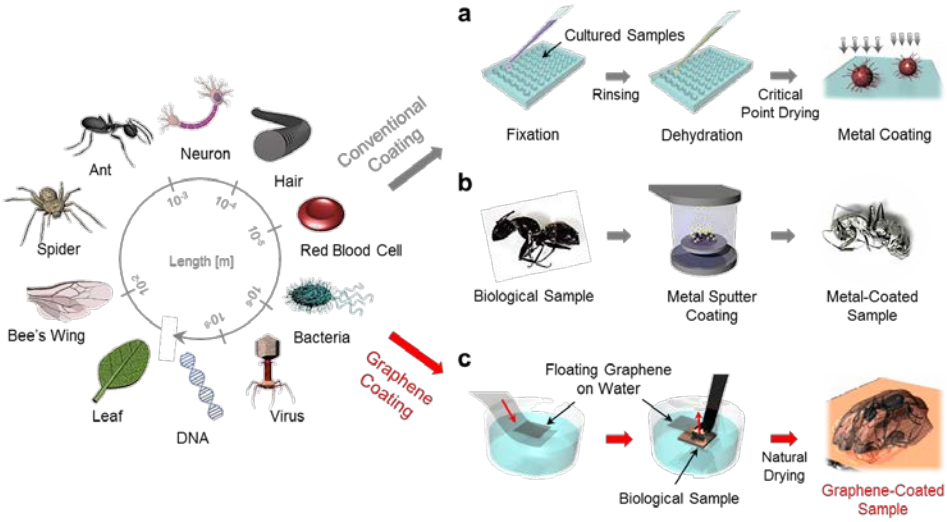

Figure 17. Schematic illustration of various biological objects in different scales and coating methods for EM analysis. a and b, Conventional coating methods of non-conducting biological samples. Soft biological samples such as cells and bacteria require complicated coating processes including aldehyde fixation, osmium tetroxide fixation, dehydration, critical point drying, staining, metal coating, etc. Hard-surfaced biological samples such as insects and plants are usually coated with Au, Pt by vacuum sputtering. The metal coating is simple, but it disables high-resolution imaging and analysis. c, Simple coating process using graphene floating on water surface. The ambient drying process allows the conformal coating of graphene on sample surface.

purity Cu foil using CVD method. Continuous graphene films coated with protecting polymer layers (i.e. poly(methyl methacrylate) (PMMA)) can be isolated from Cu foils and transferred to a desired surface after wet chemical etching. The number of graphene layers was controlled by repeating this transfer process (Fig. 18). We found that triple-layered (3-layer) graphene films provide both electron transparency and mechanical stability optimized for SEM analysis even without PMMA supports. For actual SEM imaging, the biological specimens were cleaned and transferred onto a metallic sample stage to facilitate electron discharge. The 3-layer graphene sheets were then transferred on top of the biological specimen by scooping from bottom side, followed by drying in a desiccator.

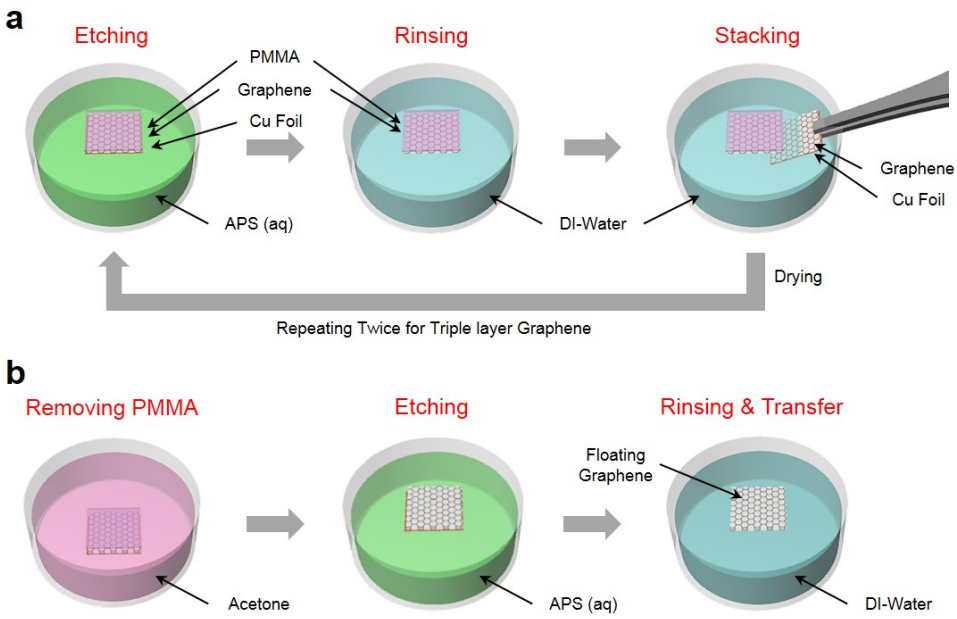

Figure 18. a and **b**, Schematic diagram showing the processes to prepare multilayer graphene films, which includes Cu etching, rinsing, and multi-stacking. After removing PMMA and etching Cu, the multiply stacked graphene layer is ready to be used for biological sample coating for EM analysis.

2.4.2. SEM imaging of various biological samples with graphene coating

To demonstrate the advantages of using graphene membrane for SEM imaging, we have selected several representative biological specimens (ants, bee's wings, water fleas, and *E. coli*) that are different in terms of size, surface hardness, and morphology. The 3-layer graphene mostly covered these millimeter to sub-micron sized samples, and only shows minor fractures caused by mechanical deformation around needle-like structures (Fig. 19). In contrast to CVD graphene coating, graphene oxide (GO) and reduced graphene oxide (rGO) coating methods resulted in inhomogeneous coating possibly due to their poor mechanical strength and difference in hydrophobicity (Fig. 20).

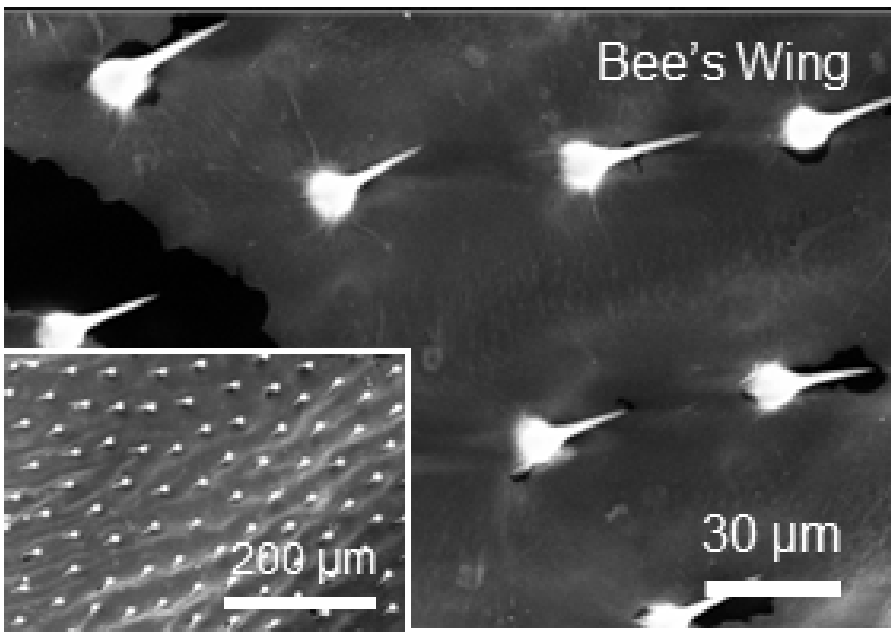

Figure 19. FE-SEM images of grapheme-coated bee's wing, where about 30 μm sized needle-like structures are uniformly arrayed.

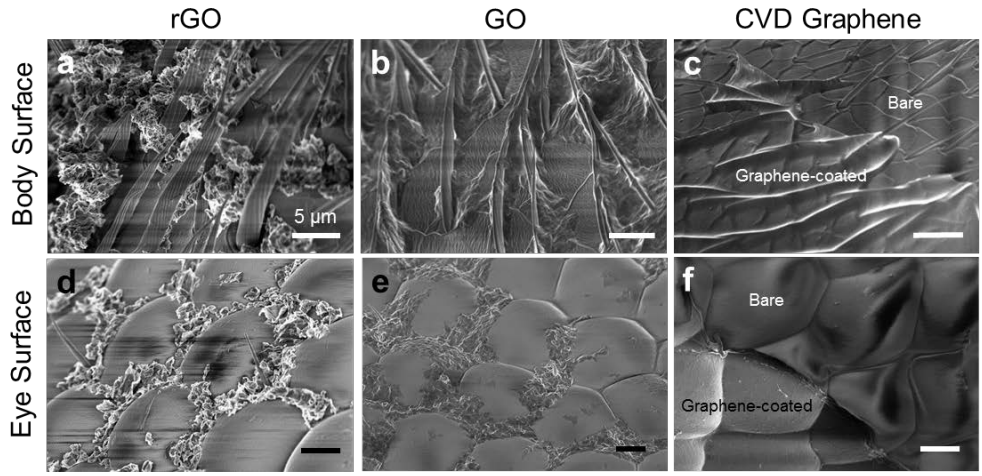

Figure 20. Comparison between reduced graphene oxide (rGO), graphene oxide (GO), and CVD graphene coatings for SEM imaging. a–c, FE–SEM images on the hairy body surface of an ant coated with rGO, GO, and 3–layer CVD graphene, respectively. Scale bars, 5 μm. The rGO and GO coated samples were prepared by dipping in 0.1 wt% rGO and GO solution for 24 hours, respectively. Both rGO and GO flakes didn't cover on the sample surface, resulting in heavy charging on the surface during SEM observation. d–f, FE–SEM images of ant's eyes coated with rGO, GO, and 3–layer CVD graphene, respectively. Scale bars, 5 μm. Acceleration voltages, 2 keV.

The high-magnification FE-SEM images of a graphene-coated ant clearly show not only unique micro-patterns but also nano-pores as small as 40 nm (Fig. 21b) that are invisible in Pt-coated samples (Fig. 21c) and amorphous carbon-coated samples (Fig. 22). Such fine and clear observation of the surface structures implies that the adhesion between graphene and the sample (mostly by van der Waals interaction) is strong enough to maintain its morphology and stable up to acceleration voltage of 20 keV (Fig. 23). The needle-like structures on bee's wings result in punctures on graphene, but the surface still shows conformal graphene coating that enables stable SEM imaging (Fig. 19). Overall, the graphene coating guarantees the high-resolution SEM imaging of nanoscale surface features close to the resolution limit of e-beam spots.

We also performed SEM imaging on a 1.5 mm long water flea (*Daphnia pulex*) covered with graphene membranes. High-magnification SEM images of the water flea (area P1 in Fig. 24b) clearly display the unique features of a water flea on

its dorsal carapace (Fig. 24). Interestingly, the graphene film mostly covers the needle-like surface on its antenna without much tearing (Fig. 24c). The advantages of graphene coating compared with a conventional metal coating method was demonstrated under identical conditions. We observed that the bare gaster surface of an ant is strongly charged even at low acceleration voltages (< 2 keV) (Fig. 25), and the bare eye surface is immediately burning at 5 keV, while the graphene-coated area doesn't show any damage even with high acceleration voltages up to 20 keV (Figs. 25 and 26).

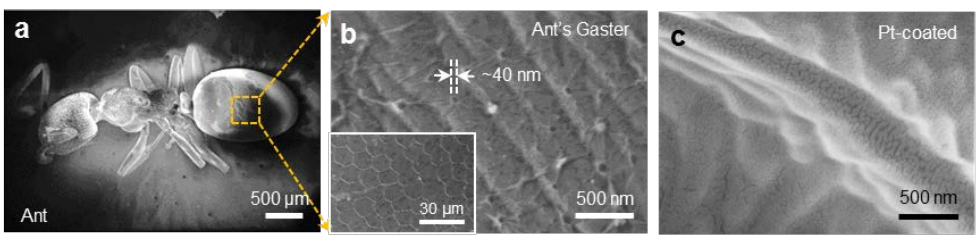

Figure 21. SEM images of various biological samples covered with graphene films. a and b, Low- and high-magnified SEM images of a graphene-coated ant. c, High-magnified SEM image of Pt-coated ant. The graphene coating enables the stable SEM imaging of sub-10 nm features on the surface, while the Pt-coated sample shows distorted morphology covered with Pt nanoparticles.

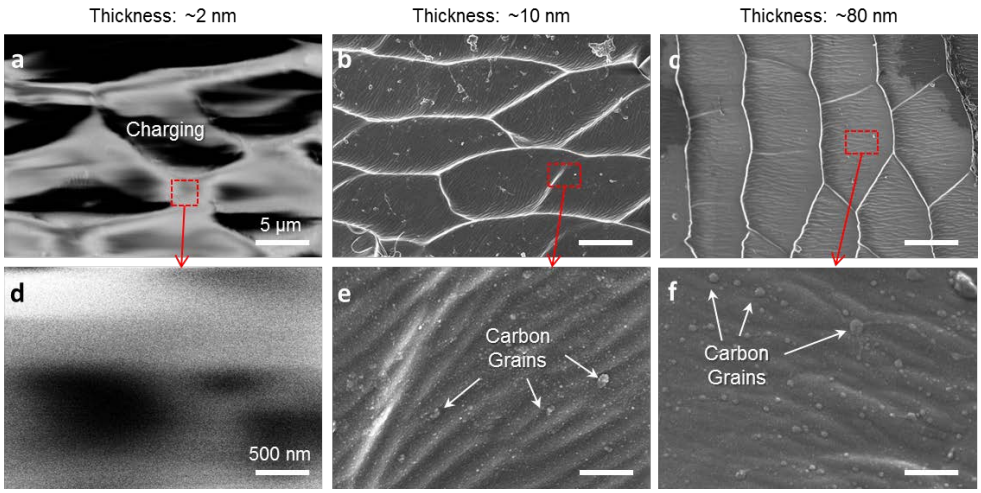

Figure 22. **a–c**, Low–magnification FE–SEM images of amorphous carbon–coated ants with different thickness of 2, 10 and 80 nm. Scale bars, 5 μm. **d–f**, High–magnification FE–SEM images of amorphous carbon–coated ants with different thickness of 2, 10 and 80 nm. Scale bars, 500 nm. 2 nanometer–thick carbon film doesn't show good coverage, and it was impossible to obtain high resolution SEM images due to severe charging and blurring effect (a and d). As the thickness of carbon films increased to 10 and 80 nm, which are normally used for observation of biological specimens, the surface morphology of carbon coated ants was visible at low magnification (b and c). However, at high magnification, sample's fine surface structure at nanometer scale was

hampered because the surface features smaller than carbon grain size cannot be imaged properly (e and f).

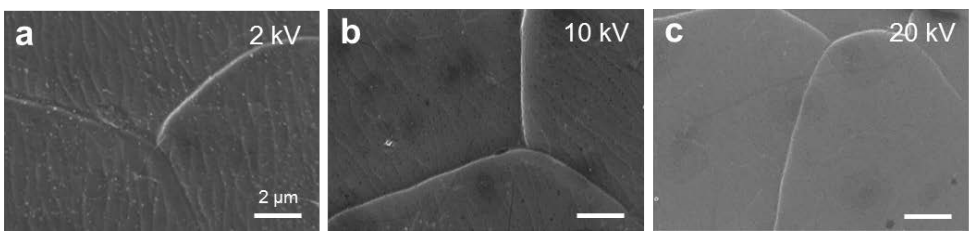

Figure 23. FE-SEM images of the graphene-coated ant (gaster) with increasing acceleration voltage from 2 to 20 keV. No damage was observed even at 20 keV. Scale bars, 2 μm.

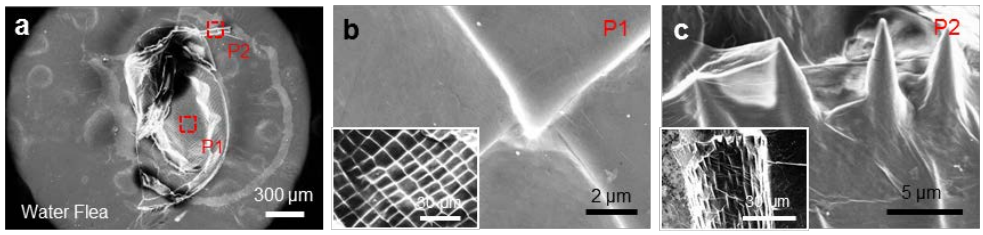

Figure 24. Low- and high-magnified SEM images of a graphene-coated water flea, respectively. The graphene film exhibits conformal contact with the non-flat surfaces of biological samples. Acceleration voltages for A to F, 2 keV.

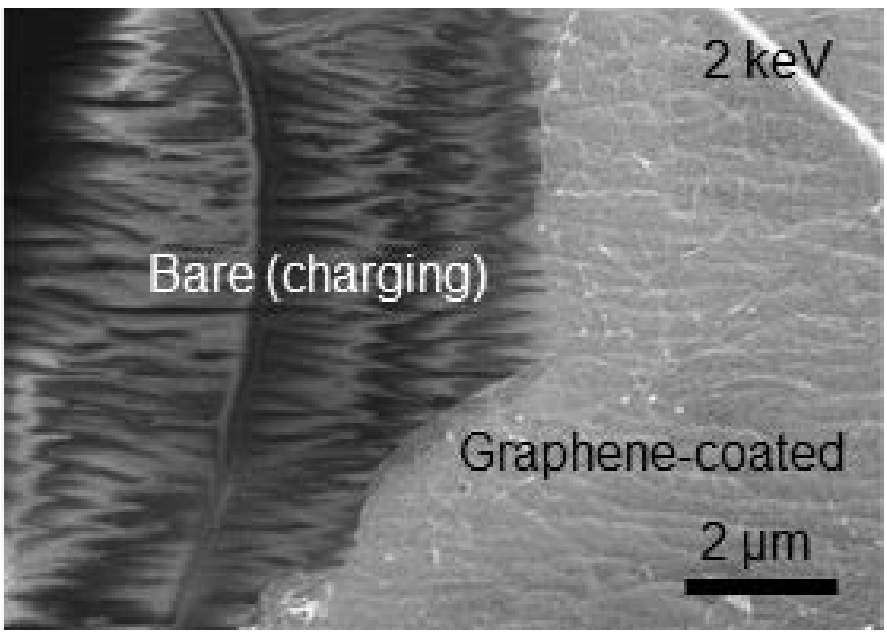

Figure 25. FE-SEM image of graphene-coated gaster surface of ant at 2 keV. Scale bar, 2 μm.

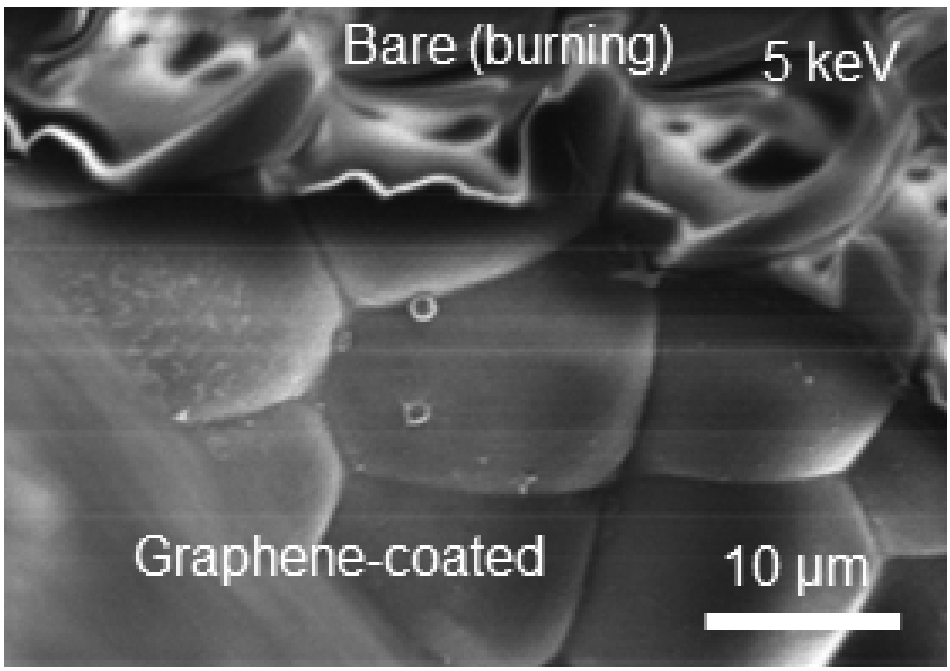

Figure 26. FE-SEM image of graphene-coated eye surface of ant at 5 keV. Scale bar, 10 μm.

Unlike the above mentioned hard-surfaced insects, soft biological objects such as living cells and bacteria need to be treated with aldehyde fixation, osmium tetroxide staining, and critical point drying processes for SEM imaging, which often distorts the sample contents and disables further qualitative or quantitative chemical analyses. In this regard, the simple graphene-coating method is advantageous because biological samples close to their native structures can be imaged and preserved for further analyses. We demonstrate that a common bacteria, *E. coli*, cultured in a liquid medium can be imaged after graphene-coating that protects *E. coli* from sudden vacuum drying as well as e-beam damage (Fig. 27) in SEM. Another graphene layer on bottom side was used to seal the liquid environment by π-π interaction with top graphene layers. It is difficult to characterize the structures of deoxyribonucleic acids (DNAs) by SEM because of their vulnerability to e-beam radiation and dehydration at vacuum. Figs. 2m-o demonstrate that DNA supercoiled structures can be visualized with graphene coating that maintains native-like structures of DNAs by encapsulating surrounding water layers.

We suppose that strong contrast in SEM images comes from charging of the surrounding water layers rather than DNA itself, which can be evidenced by no contrast in the cracked region without water layers (Fig. 25).

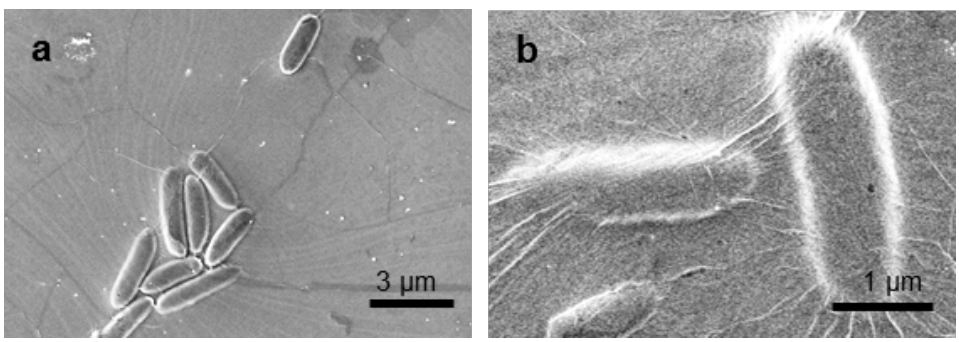

Figure 27. Low- and high-magnification SEM images obtained with acceleration voltage at 2 keV. Internal body fluids of *E. coli* with monolayer graphene are preserved at vacuum condition. Scale bars, 3 and 1 μm, respectively.

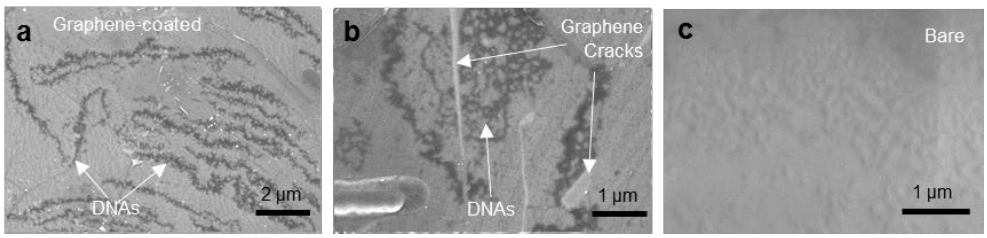

Figure 28. a and **b**, Low and high magnification SEM images of graphene-coated DNAs from E. coli, respectively. **c**, SEM image of DNAs without the graphene coating (bare) on Si wafer at 2 keV.

2.4.3. EDS analysis of graphene-coated biological samples

Furthermore, we compared the performances of graphene-coating and Pt-coating methods in chemical analysis by energy dispersive spectroscopy (EDS). All the experimental conditions and parameters including spot sizes and signal collection time were identical. The results show that EDS signals from graphene-coated samples (Fig. 29a) are 2~3 times stronger than Pt-coated samples (Fig. 29b), which facilitates the qualitative and quantitative chemical analyses on, for example, nitrogen-containing chitin (from ants) and oxygen-rich cellulose (from leaves) (Fig. 30).

The non-destructive analysis enabled by graphene coating is particularly effective for element-specific EDS mapping. The water flea sample was fed on sub-25 nm cerium oxide nanoparticles (CeO_2 NPs) to stain its digestive pathway. The CeO_2 NPs are clearly visualized in the Ce-selective EDS mapping of the graphene-coated ant, while the Pt-coated ant doesn't shows clear EDS signals (Figs. 31 and 32). The other EDS analyses also indicate that the graphene-

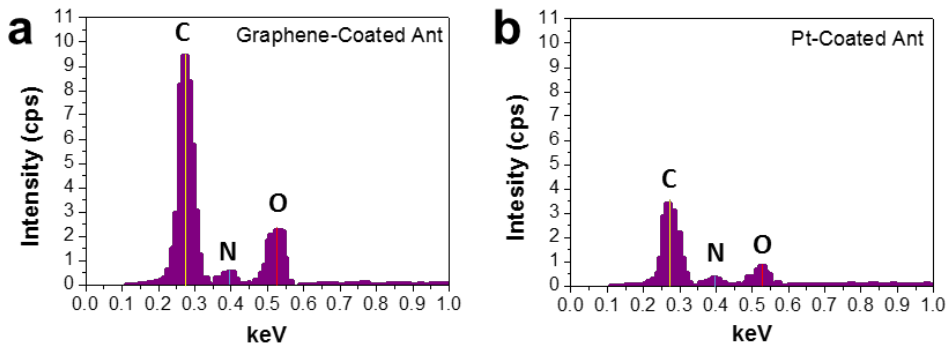

Figure 29. a and b, EDS spectra of graphene- and Pt-coated ant, respectively. Accelerating voltage, 10 keV.

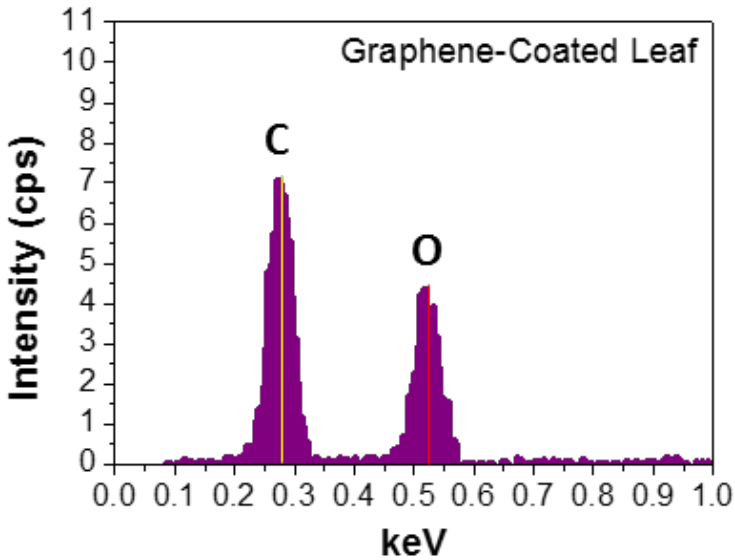

Figure 30. EDS spectra of spectra of graphene-coated leaf. Accelerating voltage, 10 keV.

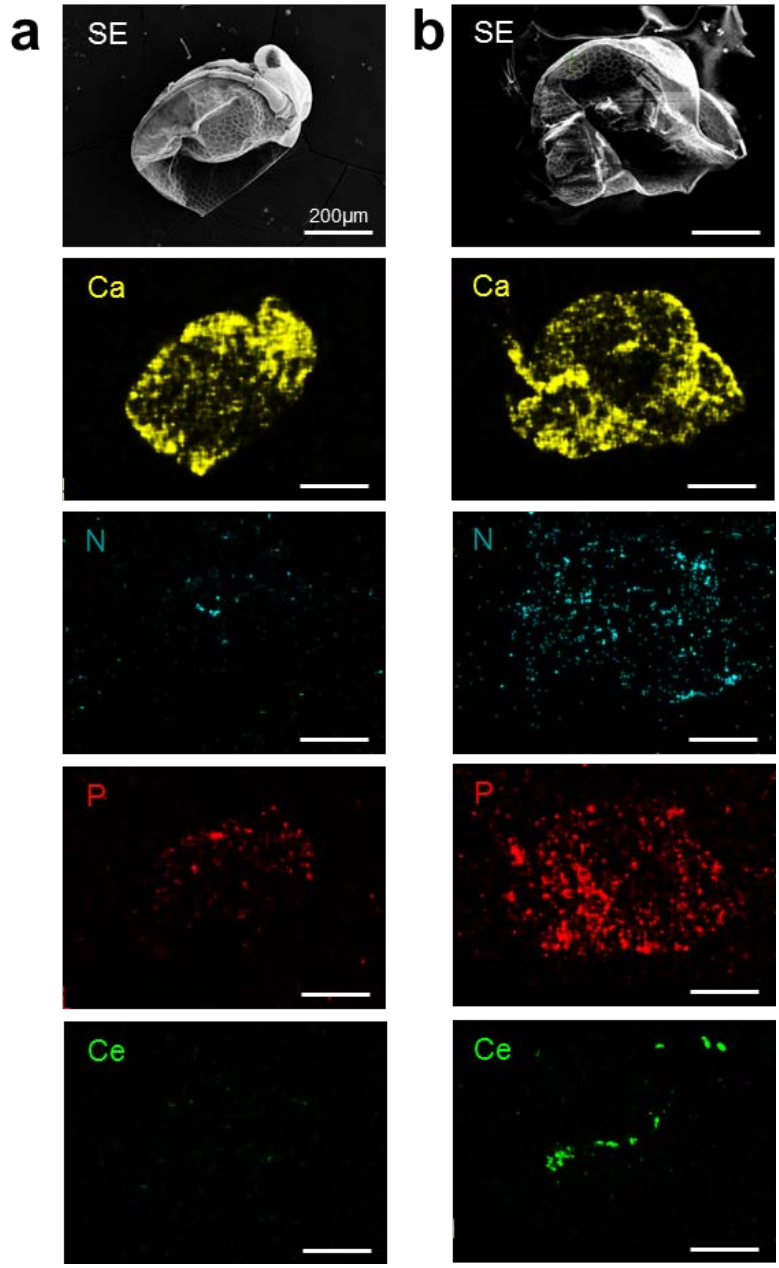

Figure 31. Representative SEM and EDS mapping images of a graphene-coated water flea and a Pt-coated water flea. Acceleration voltages, 20 keV. Scale bars, 200 μm.

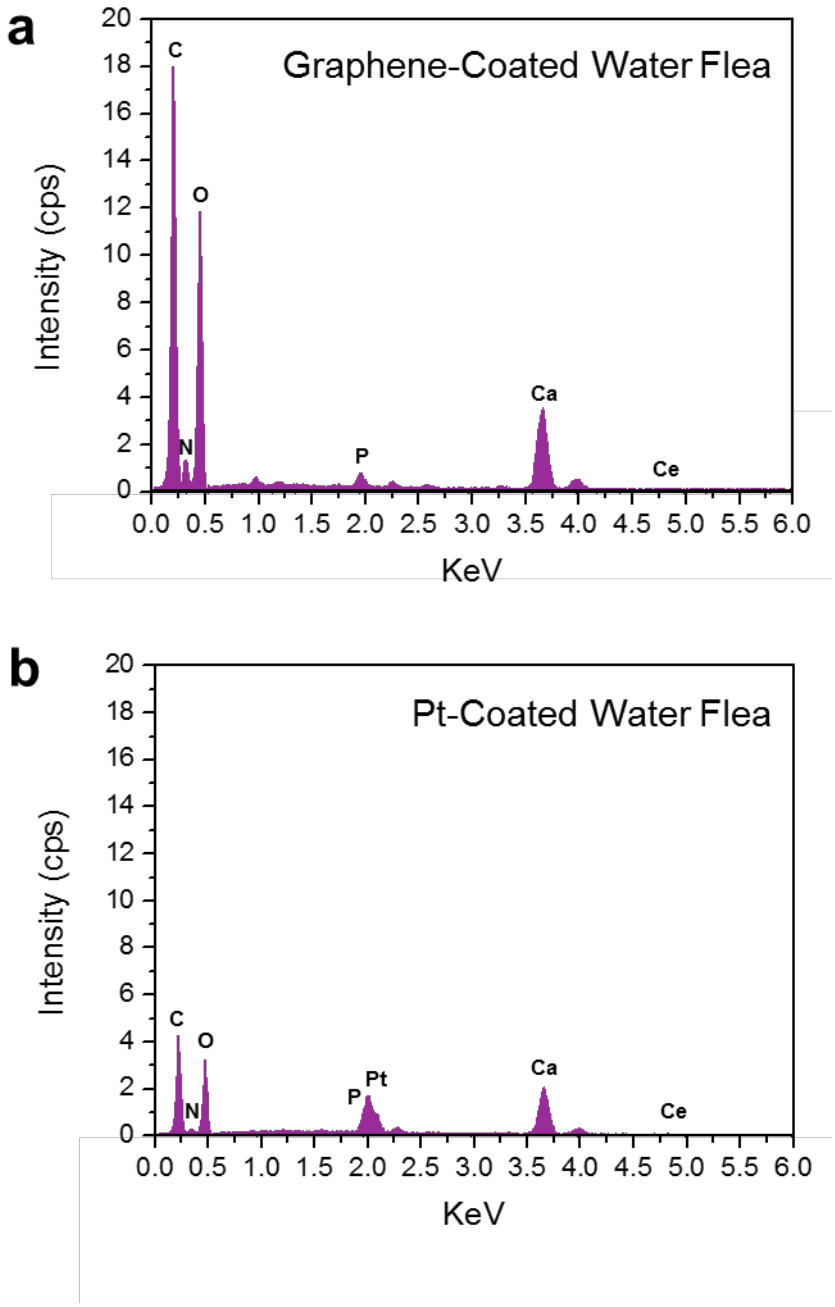

Figure 32. a and b, EDS spectra of graphene-coated and Pt-coated water fleas fed on CeO2 nanoparticles, respectively. Acceleration voltages, 20 keV.

coated method is superior to Pt-coating in terms of signal intensity. We attribute the signal reduction in Pt-coated samples to the absorption and scattering of incident electrons and X-ray fluorescence radiation by thick Pt layers, which will be further discussed in the next chapter.

2.4.4. Theoretical analysis by Monte Carlo simulations

The outstanding performance of atomically thin graphene membrane as protective coating for EM analysis was theoretically confirmed by Monte Carlo simulations (please see supplementary materials for detailed methods). The 1 nm graphene-coated chitin (Gr/Chitin) was compared with 10 nm Pt coated chitin (Pt/Chitin). As seen in the electron trajectory images (Fig. 33), incident electrons can easily pass through the thin graphene and penetrate deep into the chitin layer, while the Pt layer blocks electron penetration because of the large nucleus radius (i.e. large electron scattering cross-section) of Pt (Z=78) (Fig. 34). As the acceleration voltage increases from 2 keV to 10 keV, the maximum penetration depth of electrons increased from 140 nm to 2,250 nm for

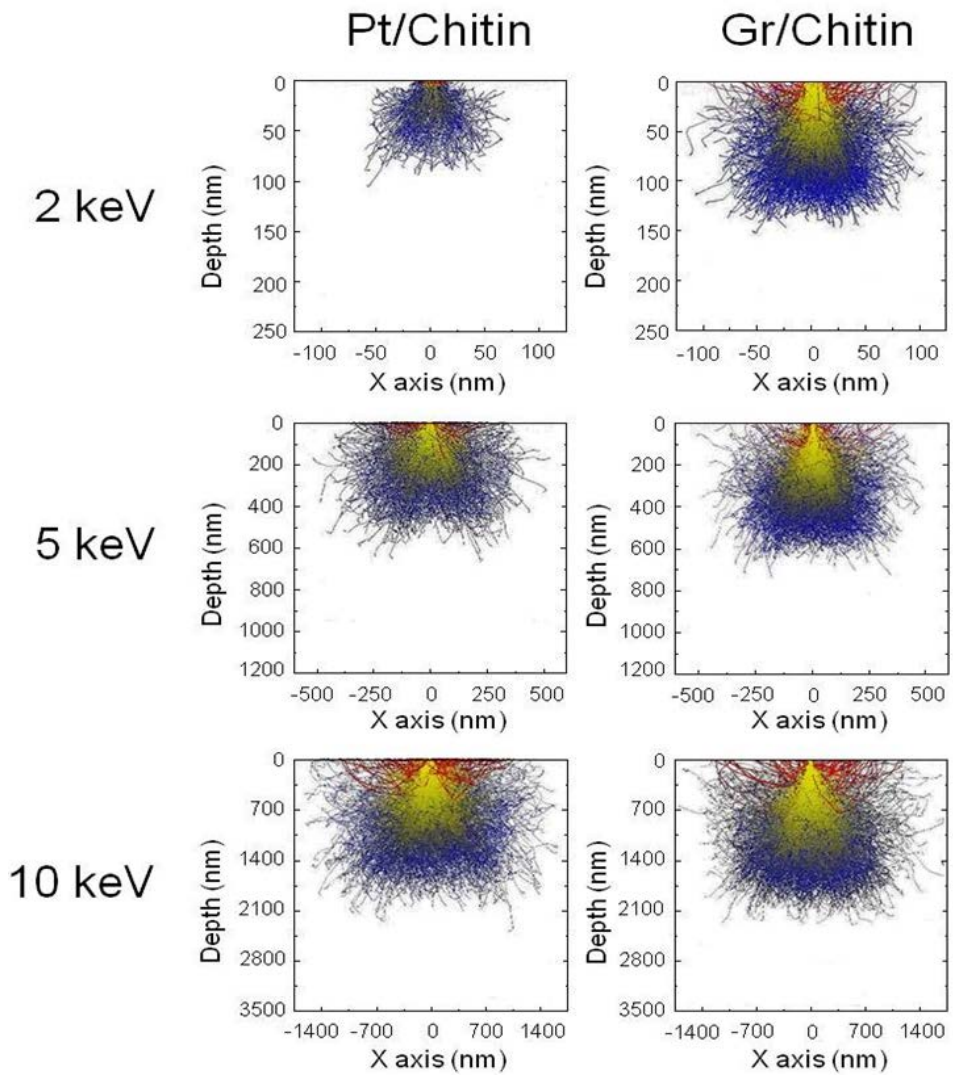

Figure 33. Electron trajectories of Pt/Chitin and Gr/Chitin. Blue lines are the trajectories of electron absorbed in the samples. Red lines are the trajectories of back scattered electron that would escape sample surface.

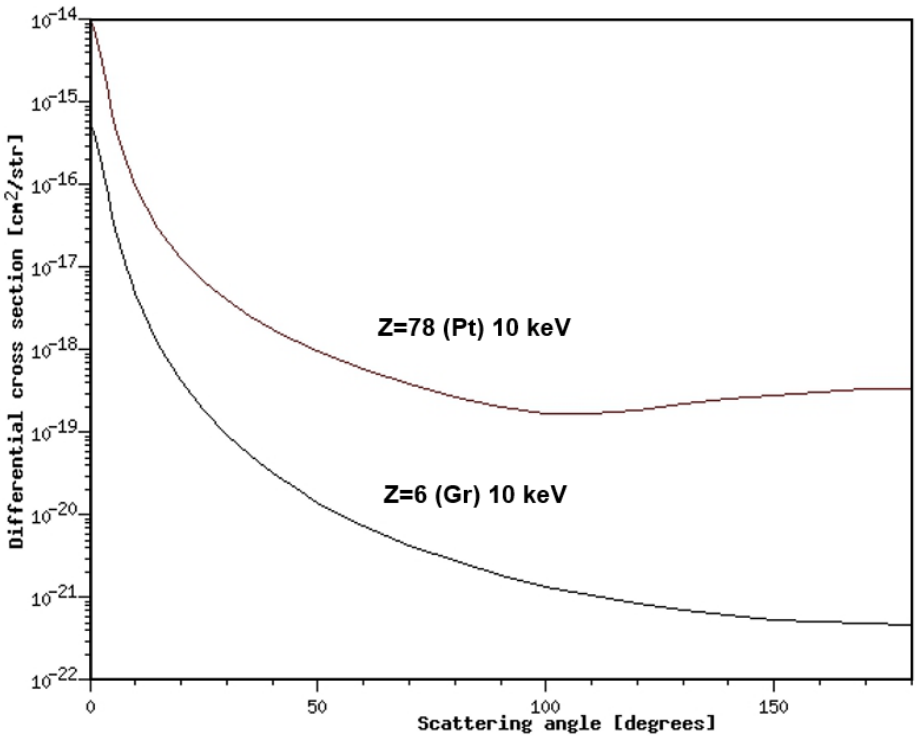

Figure 34. Differential cross section of incident electrons (10 keV) with respect to scattering angles for carbon (Z=6) and platinum (Z=78).

Gr/Chitin. This indicates that graphene membrane is more transparent to lower accelerating voltages. On the contrary, the electrons irradiated to Pt/Chitin show less penetration depths with larger scattering angles. The amount of penetrated electrons is directly related to the X-ray signals (Fig. 35), resulting in large difference in X-ray absorption intensity between Gr/Chitin and Pt/Chitin. Fig. 36 shows the cross-section profiles of energy loss along the simulated electron trajectories, which is related to the intensity of EDS signals. From 2 keV and 5 keV, most of the energy loss happens inside the 10 nm Pt layer. Major energy loss still occurs near the Pt layer at 10 keV. On the other hand, energy loss in Gr/Chitin mostly takes place inside the chitin layer even at 2 keV, indicating that the graphene is almost free from electron energy loss and background EDS signals. Figure 35 shows the depth profiles of Rho-Z X-ray intensity of carbon for Gr/Chitin (red) and Pt/Chitin (grey). As the accelerating voltage increases from 2 keV to 10 keV, the total X-ray intensities for Pt/Chitin and Gr/Chitin increased from 6 to 259 and from 87 to 470, respectively (see also Fig. 37) for the

simulations for nitrogen and oxygen analysis). This indicates that graphene is superior to Pt for protective coating for EDS analysis. The experimental EDS spectra with varying accelerating voltages coincide with the simulation results (Figs. 38 and 39).

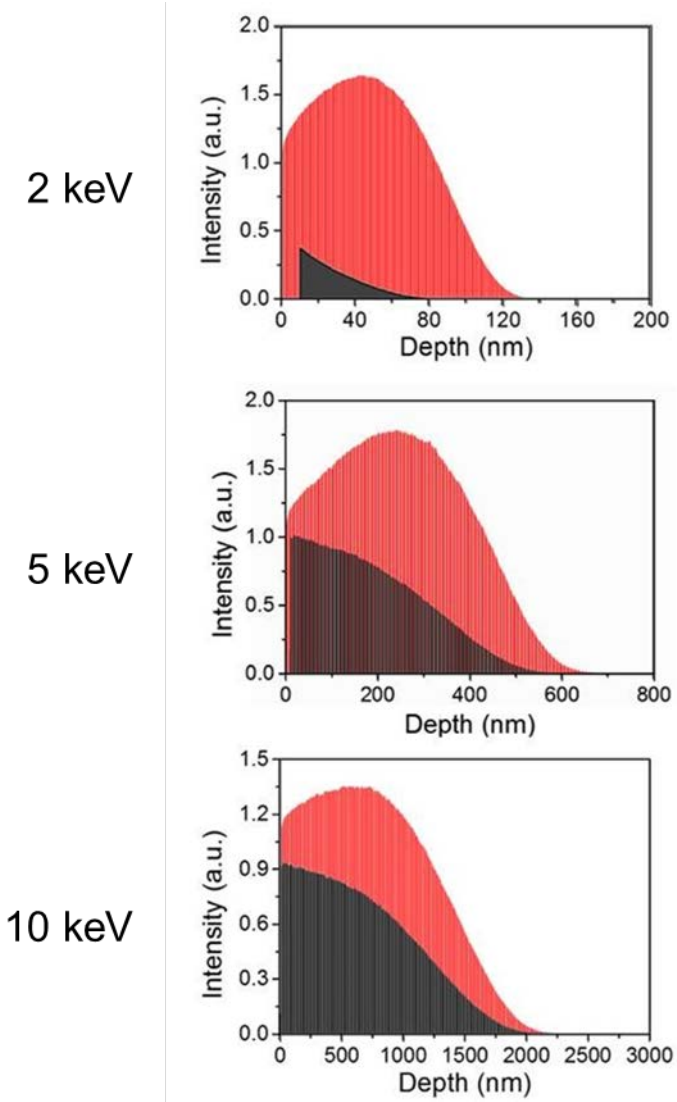

Figure 35. Phi Rho−Z X−ray absorbed intensity of carbon (Phi = X−ray generation function, Rho−Z = a way of plot generation per unit density). Red and dark grey areas show the total intensities of Gr/Chitin and Pt/Chitin, respectively. The absorbed intensity of the Gr/Chitin are 87, 290, and 470 at 2, 5, and 10 keV, respectively. The intensity of Pt/Chitin are 6, 116, and 259 at 2, 5, and 10 keV, respectively.

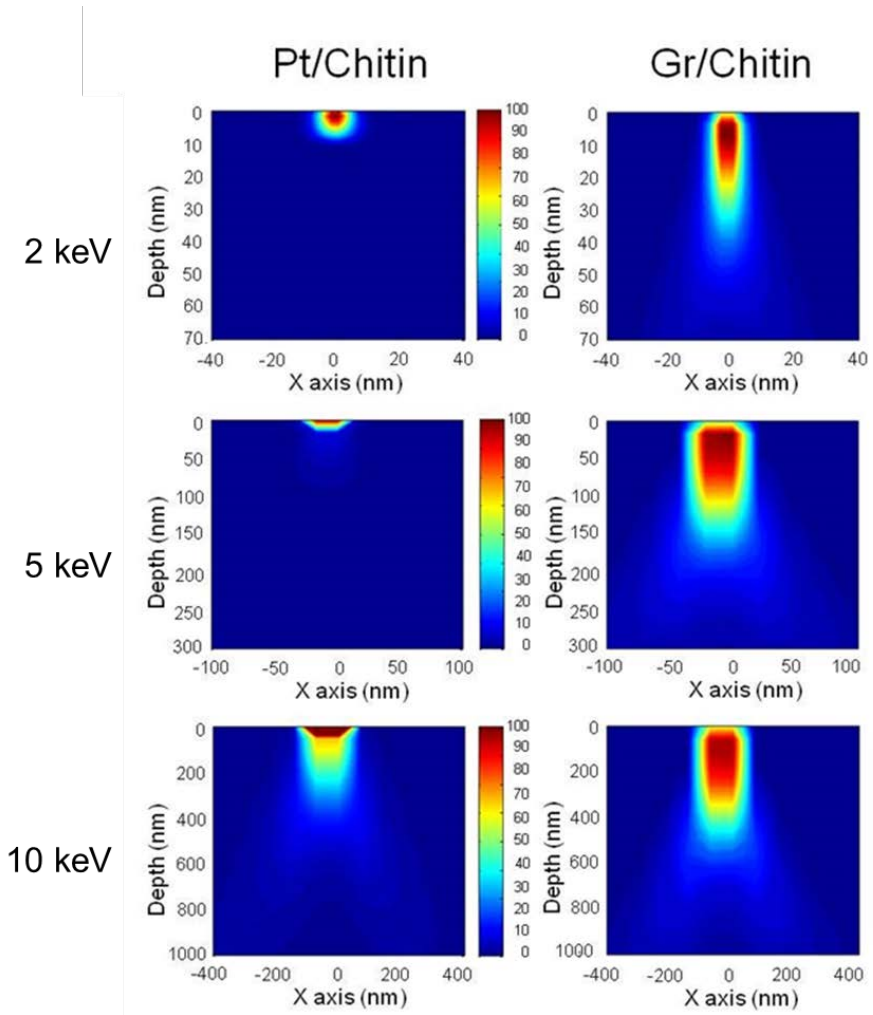

Figure 36. Energy distribution contour mapping images of Pt/Chitin and Gr/Chitin. Dark red and dark blue are 100 and 0, respectively.

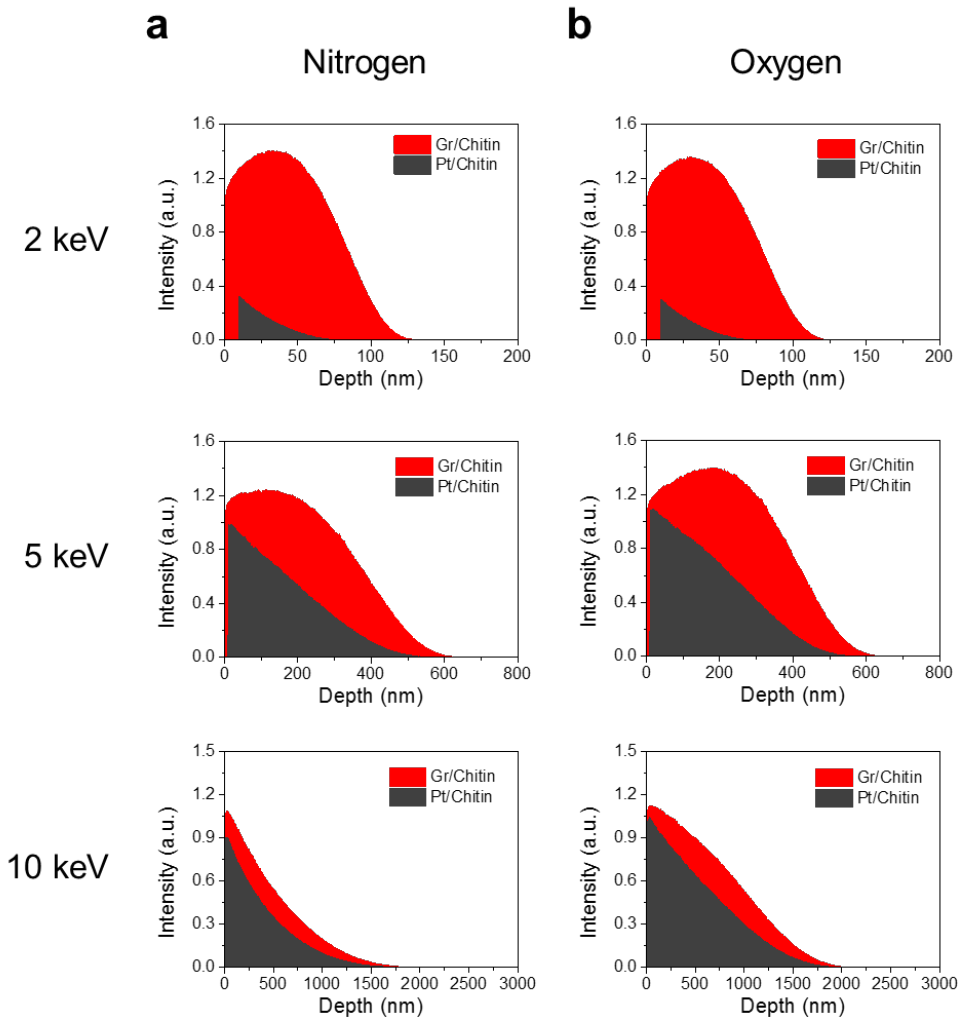

Figure 37. X-ray intensities of nitrogen (**a**) and oxygen (**b**) calculated by Monte Carlo simulation with different accelerating voltages. The red and grey areas show the absorbed X-ray intensity by Gr/Chitin and Pt/Chitin, respectively. The intensities of nitrogen in Gr/Chitin and Pt/Chitin are 11/31/29 and 0.74/14/19 at 2/5/10 keV, respectively. The intensities of oxygen in Gr/Chitin and

Pt/Chitin are 83/338/452 and 5/162/312 at 2/5/10 keV, respectively.

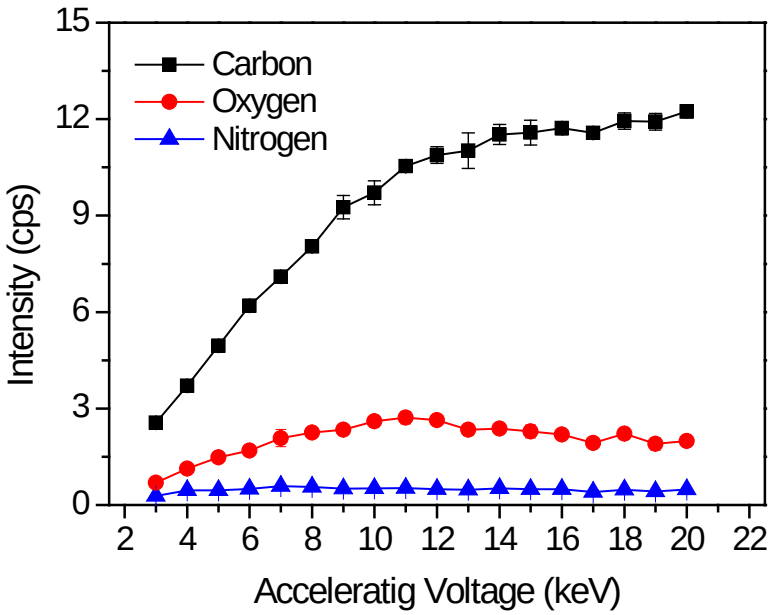

Figure 38. EDS signal intensities of graphene-coated ant with increasing acceleration voltages from 3 keV to 20 keV. Working distance and accumulation time were 8.5 mm and 40 seconds, respectively.

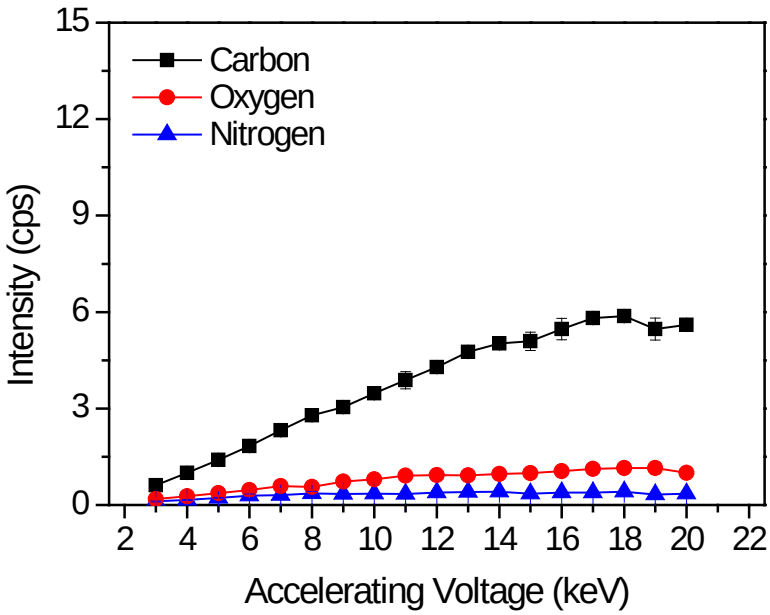

Figure 39. EDS signal intensities of Pt-coated ant with increasing acceleration voltages from 3 keV to 20 keV. Working distance and accumulation time were 8.5 mm and 40 seconds, respectively.

3.5. Conclusion

In conclusion, we demonstrated that graphene's outstanding mechanical strength, conductivity, flexibility, and transparency to electron beams enable the simple and nondestructive imaging and analysis of various biological samples with high resolution that can be hardly achieved in bare or metal-coated samples. The graphene coating effectively prevent charge accumulation by spreading e-beam induced charges and heats over large surface area, and the high mechanical strength and flexibility of graphene allows conformal coating by excellent adhesion with various biological interfaces. We believe that the graphene-coated imaging and analysis would provide us a new opportunity to explore various biological phenomena unseen before due to the limitation in sample preparation and image resolution, which will broaden our understanding on the life mechanism of various living organisms.

3.6. References

1. Hayat, M. A., Principles and techniques of electron microscopy: Biological applications (Cambridge University Press, Cambridge, UK; New York, ed. 4th, 2000).
2. Fratzl, P. Cellulose and collagen: From fibres to tissues. Curr. Opin. *Colloid Interface Sci.* **8**, 32–39 (2003).
3. Lucic, V., Forster, F., Baumeister, W. Structural studies by electron tomography: From cells to molecules. *Annu. Rev. Biochem.* **74**, 833–865 (2005).
3. Midgley, P. A., Ward, E. P. W., Hungria, A. B., Thomas, J. M. Nanotomography in the chemical, biological and materials sciences. *Chem. Soc. Rev.* **36**, 1477–1494 (2007).
4. Egerton, P. A. Physical principles of electron microscopy: An introduction to TEM, SEM, and AEM (Springer Science, New York, 2005).
5. Joy, D. C., Romig, A. D., Goldstein, J. Principles of analytical electron microscopy. (Plenum Press, New York, 1986).
6. Brydson, R. Electron energy loss spectroscopy. (Bios in

association with the Royal Microscopical Society, Oxford, 2001).

7. Royall, C. P., Thiel, B. L. Radiation damage of water in environmental scanning electron microscopy. *J. Microsc.-Oxford* **204**, 185-195 (2001).

8. Parsons, D. F. An electron microsocpe study of radiation damage in the mouse oocyte. *J. Cell Biol.* **14**, 31-48 (1962).

9. Gibson, J. B., Goland, A. N., Milgram, M., Vineyard, G. H. Dynamics of radiation damage. *Phys. Rev.* **120**, 1229-1253 (1960).

10. Isaacson, M., Jonson, D., Crewe, A. V. Electron beam excitation and damage of biological molecules; its implications for specimen damage in electron microscopy. *Radiat. Res.* **55**, 205-224 (1973).

11. Cosslett, V. E. Radiation damage in the high resolution electron microscopy of biological material: *A review. J. Microsc.* **113**, 113-129 (1978).

12. Bozzola, J. J., Russell, L. D. Electron Microscopy: Principles and techniques for biologists. (Jones and Bartlett, Sudbury, Mass, ed. 2nd, 1999).

13. Stokroos, I., Kalicharan, D., Van der Want, J. J. L., Jongebloed, W. L. A comparative study of thin coatings of Au/Pd, Pt and Cr produced by magnetron sputtering for FE-SEM. *J. Microsc.-Oxford* **189**, 79-89 (1998)

14. Hermann, R., Muller, M. High resolution biological scanning electron microscopy: A comparative study of low temperature metal coating techniques. *J. Electron Micr. Tech.* **18**, 40-449 (1991)

15. Reimer, L. Scanning electron microscopy: Physics of image formation and microanalysis. (Springer, Berlin; New York, ed. 2nd completely rev. and updated, 1998).

16. Geim, A. K., Novoselove, K. S. The rise of graphene. *Nat. Mater.* **6**, 183-191 (2007).

17. Lee, C., Wei, X. D., Kysar, J. W., Hone, J. Measurement of the elastic properties and intrinsic strength of monolayer graphene. *Science* **321**, 385-388 (2008).

18. Loh, K. P., Bao, Q. L., Eda, G., Chhowalla, M. The chemistry of two-dimensional layered transition metal dichalcogenide nanosheets. *Nat. Chem.* **2**, 1015-1024 (2010).

19. Meyer, J. C. et al. The structure of suspended graphene sheets. *Nature* **446**, 60–63 (2007).

20. Kim, K. S. *et al*. Large–scale pattern growth of graphene films for stretchable transparent electrodes. *Nature* **457**, 706–710 (2009).

21. Li, X. S. *et al*. Large–area synthesis of high–quality and uniform graphene films on copper foils. *Science* **324**, 1312–1314 (2009).

22. Bae, S. *et al*. Roll–to–roll production of 30–inch graphene films for transparent electrodes. *Nat. Nanotechnol.* **5**, 574–578 (2010).

23. Bae, S., Kim, J., Shin, D., Ahn, j. H., Hong, B. H. Towards industrial applications of graphene electrodes. *Phys. Scr.* T146, 014024 (2012).

24. Yuk, J. M. *et al.*, High–resolution EM of colloidal nanocrystal growth using graphene liquid cells. *Science* **336**, 61–64 (2012).

25. Radic, S. *et al*. Competitive binding of natural amphiphiles with graphene derivatives. *Sci. Rep.* **3**, 02273 (2013).

26. Drouin, D. *et al*. CASINO V2.42: A fast and easy–to–use

modeling tool for scanning electron microscopy and microanalysis users. *Scanning* **29**, 92–101 (2007).

초 록

제 1장에서는 그래핀 액체셀을 이용하여 액상에서의 나노 공기방울을 실시간으로 관찰한 연구에 대하여 설명하였다. 본 연구에서는, 두 층의 그래핀 막으로 수십~ 수백 나노미터 높이의 물 층을 가두고, 그 안에 존재하는 나노미터 크기의 공기방울을 고진공 투과전자현미경을 이용하여 관찰하였다. 관찰된 나노 공기방울은 5-15 nm 크기로 장시간 존재하는 것이 확인되었으며, 단면 TEM 관찰을 통해 60~90도의 접촉각을 갖는 렌즈 모양의 형태를 띄고 있다는 것이 확인되었다. 또한 나노 공기방울의 발생, 성장, 소멸 등의 과정을 실시간으로 관찰함으로써, 두 나노 공기방울의 상대적인 크기 차이에 따라 확연히 다른 두 가지 성장 매커니즘 (1. 경계면 붕괴 성장, 2. 유사-오스트발트 숙성 성장)이 존재한다는 것을 확인하였다. 그리고 마지막으로, 두 공기방울간의 간격이 2 nm 이하일 때, 일반적인 오스트발트 숙성 과정과 다른 직접 가스 확산 과정이 일어날 수 있음을 확인하였다. 본 연구는 자연계에 존재하는 다양한 생명현상 및 화학 촉매 작용, 잠수병과 같은 이상기체발생 현상과 같은 생명 현상을 이해하는데 도움을 줄 것으로 기대한다.

제 2장에서는 그래핀 코팅막을 이용하여 비전도성 생물시료의 비파괴적 전자현미경 분석에 관한 연구를 설명하였다. 곤충 및 식물, 세포 등 비전도성 생물시료의 주사전자현미경 분석 시 표면처리 목적으로 사용되어 온 금속 코팅막은 그 두께로 인해 10 nm 이하의 미세 표면구조를 관찰하는 것이 불가능했으며, X선 등을 이용한 원소분석 방법에서도 정확한 시료 분석을 어렵게 하는 요인으로 작용하였다. 따라서 본 연구에서는 단층 및 적층된 그래핀을 이용하여 곤충류, 식물류 및 대장균류 등의 다양한 생물학적 시료를 관찰대상으로 선택하여, 주사전자현미경 관찰 시 코팅막으로서의 그래핀의 성능을 확인하였다. 그래핀막은 이론상 원자 한 층의 두께를 갖으며 열 및 전기 전도성이 우수하기 때문에, 전자빔에 대한 방사상 피해 없이 높은 해상도에서 시료의 미세구조 관찰이 가능하였으며, 에너지 분산분석기를 이용한 원소분석 결과에서도 기존의 금속 코팅막에 비해 더 높은 민감도를 나타내는 것을 확인하였다.

주요어: 전자현미경, 나노 공기방울, 주사전자현미경, 투과전자현미경, 그래핀 액체 셀, 그래핀 코팅

학 번: 2012 – 30874